

Engineered extracellular vesicles for concurrent Anti-PDL1 immunotherapy and chemotherapy

Yundi Chen^{a,1}, Lixue Wang^{a,b,**,1}, Mingfeng Zheng^{c,1}, Chuandong Zhu^{a,b}, Guosheng Wang^a, Yiqiu Xia^d, Ethan J. Blumenthal^a, Wenjun Mao^{c,***}, Yuan Wan^{a,*}

^a The Pq Laboratory of Micro/Nano BiomeDx, Department of Biomedical Engineering, Binghamton University-SUNY, Binghamton, NY, 13902, United States

^b Department of Radiotherapy, The Second Hospital of Nanjing, Nanjing University of Chinese Medicine, Nanjing, Jiangsu, 210003, China

^c Department of Cardiothoracic Surgery, The Affiliated Wuxi People's Hospital of Nanjing Medical University, Wuxi, Jiangsu, 214023, China

^d Department of Biomedical Engineering, Carnegie Mellon University, Pittsburgh, PA, 15213, United States

ARTICLE INFO

Keywords:

CRISPR/Cas9

PD-1/PD-L1

Extracellular vesicles

Immune checkpoint inhibitors

Drug delivery

ABSTRACT

Immune checkpoint inhibitors (ICI) targeting PD-1/PD-L1 have been approved for the treatment of a variety of cancers. However, the efficacy of antibody-based ICIs could be further improved by mitigating anti-drug antibodies, proteolytic cleavage, and on-target off-tumor toxicity. One strategy for accomplishing this is through the use of extracellular vesicles (EVs), cell derived submicron vesicles with many unique properties. We constructed an engineered MDA-MB-231 cell line for harvesting EVs. This was accomplished by overexpressing a high-affinity variant human PD-1 protein (havPD-1), while simultaneously knocking out intrinsic PD-L1 and beta-2 microglobulin. The engineered havPD-1 EVs reduced PD-L1 overexpressing cancer cell proliferation and induced cellular apoptosis. Moreover, the EVs were shown to efficiently block PD-L1 mediated T cell suppression. Meanwhile antibody-dependent cellular cytotoxicity and complement-dependent cytotoxicity were not observed. The havPD-1 EVs treatment resulted in robust anti-tumor activity in both preventative co-implantation and therapeutic xenograft tumor models reconstituted with human T cells. The efficacy of the havPD-1 EVs was shown to be comparable to clinical anti-PD1 monoclonal antibodies. Additionally, loading the havPD-1 EVs with a potent PARP inhibitor was shown to further augment treatment efficacy. In brief, the engineered universal EVs harboring havPD-1 proteins can be used for cancer concurrent immunotherapy and chemotherapy.

1. Introduction

Immune checkpoint inhibitors (ICI) targeting PD-1/PD-L1 have revolutionized the treatment of many cancers [1]. Humanized monoclonal antibodies (mAb) can efficiently block checkpoint proteins from binding with their partner proteins, thus allowing tumor-infiltrating cytotoxic T cells to recognize and kill tumor cells [2]. Preclinical and clinical studies further confirm that chemotherapy combined with ICIs synergistically facilitate anti-tumor immune responses and improve survival in a subset of patients [3–5]. However, the deglycosylation of mAbs or other molecular engineering processes may result in mAb aggregation, which can trigger production of anti-drug antibodies (ADA)

that neutralize the therapeutic effect of mAbs and, in rare cases, induce adverse effects [6]. Moreover, free therapeutic anti-PD-1 or anti-PD-L1 mAbs are vulnerable to being cleaved by proteases *in vivo*, which leads to mAb inactivation and elimination [7]. Furthermore, moderate to severe on-target off-tumor toxicity that come with a large-dose of mAbs may deter patients [8]. Last but not least, mAb ICIs require a complex manufacturing process, high production costs, and challenging storage conditions. In brief, the treatment efficacy of PD-1/PD-L1 targeting therapeutic agents could be improved by addressing or mitigating ADA, proteolytic cleavage, and on-target off-tumor toxicity, as well as developing simplified manufacturing processes.

Extracellular vesicles (EVs) are sub-micrometer sized lipid bilayer-

Peer review under responsibility of KeAi Communications Co., Ltd.

* Corresponding author. 65 Murray Hill Road, Biotechnology Building, BI2625, Binghamton University, Vestal, NY, 13850, USA.

** Corresponding author. 1-1 Zhongfu Road, Naning, Jiangsu, 210003, China.

*** Corresponding author. 299 Qingyang Road, Wuxi, Jiangsu, 214023, China.

E-mail addresses: lixue.wang@njucm.edu.cn (L. Wang), maowenjun1@njmu.edu.cn (W. Mao), ywan@binghamton.edu (Y. Wan).

¹ Equal contribution.

<https://doi.org/10.1016/j.bioactmat.2021.07.012>

Received 7 June 2021; Received in revised form 12 July 2021; Accepted 13 July 2021

Available online 21 July 2021

2452-199X/© 2021 The Authors. Publishing services by Elsevier B.V. on behalf of KeAi Communications Co. Ltd. This is an open access article under the CC

BY-NC-ND license (<http://creativecommons.org/licenses/by-nc-nd/4.0/>).

enclosed vesicles that are released by various cells [9]. While still in its infancy, the field of EV-based therapeutic agents has been rapidly growing. In cancer therapy, EVs have many unique properties that have made them exceptionally useful as drug delivery nanocarriers [10], cancer vaccines [11], and antigen conferrers [12]. In contrast with commercial liposomes and polymeric nanoparticles, EVs are a natural delivery system that can evade phagocytosis, have extended circulatory half-life, and exhibit excellent biocompatibility without potential long-term safety issues [13,14]. The lipid envelop can retard metabolism of EV cargo by limiting the access of nucleases and proteases [15]. Furthermore, EVs generated by certain cells can achieve tumor- or tissue-specific delivery. For example, tumor-derived EVs contain membrane proteins and lipids representative of parental cells which preferentially fuse with homotypic cells, and thus enabling tumor-selective drug delivery [16]. The small size of EVs facilitates their extravasation, translocation through physical barriers, and passage through extracellular matrix [17]. Furthermore, EVs can fuse with the cellular plasma membrane and deliver drugs directly into cytoplasm, thereby evading lysosomal destruction of vulnerable cargo molecules [18]. It is noteworthy that clinical-grade EVs for cancer treatment have been produced at a large scale under GMP conditions [19,20]. Together, these features position EV technology to be rapidly translated into clinical practice.

Herein, we report the preparation and therapeutic use of high-affinity variant human PD-1 (havPD-1) overexpressing EVs as ICLs and as drug nanocarriers for concurrent immunotherapy and chemotherapy (Fig. 1). It is the first attempt to develop havPD-1 overexpressing EVs (havPD-1 EV) as direct immunotherapeutic agents. This accomplishment required the construction of a MDA-MB-231 cell line that is devoid of human leukocyte antigen class I (HLA-I) and PD-L1, while overexpressing a high affinity PD-1 variant (havPD-1). EVs derived from this cell line were shown to exhibit significant anti-tumor efficacy in xenograft models that contain human T-cells. Further, we show that chemotherapeutic agents can be loaded into the derived havPD-1 EVs for combination therapy. Our findings reveal that havPD-1 EVs can neutralize tumor derived PD-L1 EVs, directly induce apoptosis in PD-L1 overexpressing tumor cells, and efficiently activate cytotoxic T cells. We show that monotherapy using havPD-1 EVs *in vivo* results in a cytostatic effect that is comparable with that of Atezolizumab, while the

combination therapy with encapsulated low-dose PARP inhibitors results in significant tumor regression.

2. Materials and methods

2.1. Generation of B2M^{KO}/PD-L1^{KO}/high-affinity variant PD-1 knock-in/CD81-GFP fusion MDA-MB-231 cell line

(B2M) knockout/PD-L1 knockout MDA-MB-231 cells (MDA-MB-231-PD-L1^{KO}) were established using CRISPR/Cas9. The guide sequence (5'-ATT TAC TGT CAC GGT TCC CA-3') specific to human B7-H1 exon 3, and guide sequence (5'-CGC GAG CAC AGC TAA GGC CA CGG-3') specific to human B2M exon 1 were used [21,22]. Experimental details can be found elsewhere [22]. Cells were sorted and subcloned for the following studies. Cells were labeled with Atezolizumab and secondary antibody (Biolegend, 409304) followed by characterization with flow cytometry. Further experimental details can be found elsewhere [23]. The full sequence of high-affinity variant PD-1 (havPD-1) was reported elsewhere [24]. We purposely truncated the cytoplasmic domain of havPD-1 and fully preserved extracellular and transmembrane domains. The following amino acid sequence of truncated havPD-1 containing only five amino acid residues (underlined) of the cytoplasmic domain was used to generate codon: MQIPQAPWVP VWAVLQLGWR PGWFLDSPDR PWNPPTFSPA LLVVTEGDNA TFCFSFNST ESFHVIVHRE SPSGQTDTLA AFPEDRSQPG QDARFRVTQL PNGRDFHMSV VRARRNDSGT YVCGVISLAP KIQIKESLRA ELRVTERRAE VPTAHPSPP RPAGQFQTLV VGVVGGLLGS LVLVWVLA V ICSRAA. Kozak sequence (GCC ACC) and signal peptide sequence of human PD-1 (5'-ATG CAA ATA CCA CAG GCT CCT TGG CCT GTT GTT TGG GCA GTT CTC CAG CTG GGA TGG AGG CCA GGA TGG-3') were included. MDA-MB-231-PD-L1^{KO} cells were transduced with packaged lentivirus. Cells were labeled with anti-PD-1 antibodies (Biolegend, 329906) and sorted by flow cytometry. The expression level of havPD-1 was measured with quantitative flow cytometry. To facilitate EV visualization and tracking, we further constructed PD-L1^{KO} havPD-1 knock-in CD81-GFP fusion MDA-MB-231 cells which can steadily release havPD-1 EVs expressing CD81-GFP. The C-terminal fusion expression vector of human tetraspanin CD81 with GFP was configured as following: CMV

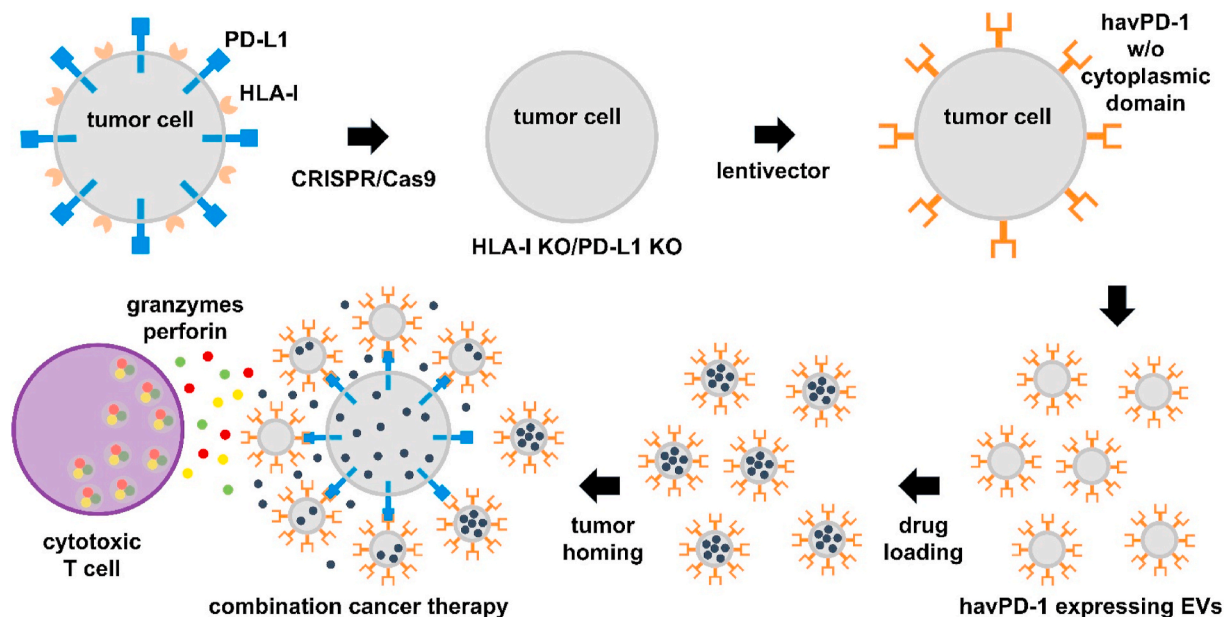


Fig. 1. Schematic of havPD-1 overexpressing EVs for concurrent immunotherapy and chemotherapy. Instinct B2M and PD-L1 are knocked out using CRISPR/Cas 9 followed by overexpressing truncated havPD-1 proteins on cell membranes. The derived havPD-1 expressing EVs are harvested from cell culture supernatant and further loaded with small molecular drugs, e.g., PARP inhibitors, for homotypic drug delivery. The interaction and blockade PD-L1 on target cells with havPD-1 can activate cytotoxic T cells, deliver encapsulated drugs to cytosol, and directly induce apoptosis in recipient cells.

promoter, CD81, linker between CD81 and GFP, GFP, and $3 \times$ FLAG tag. The constructed pLVX-CMV-PGK-Hygro plasmid was used, and cells were transduced with packaged lentivirus vectors. Subsequently, cells were incubated with 400 μ g/ml hygromycin for 72 h to enrich hygromycin-resistant cells.

2.2. Generation of MDA-MB-231-tdTomato cell lines

MDA-MB-231 cells bearing an intrinsic fluorescent membrane tdTomato (MDA-MB-231-tdTomato) were constructed. A detailed protocol can be found elsewhere [25]. In brief, palmitoylation sequences (MLCCMRRTKQ) of growth cone-associated protein (GAP43) were genetically fused in-frame to the N-terminus of tdTomato. The Palmito-Tomato sequence was inserted at the NheI and XhoI sites of CSCGW2 lentivector plasmid. The constructs allow tdTomato to have S-palmitoylation through a thioester linkage between the sulfhydryl groups on the cysteines of the palmitoylation signal. The palmitoylated tdTomato is synthesized in the transfected cells and the palmitoylated fluorescent protein is automatically integrated into the plasma membrane via the lipid tail. Cells were stably transduced with packaged lentivirus vectors (MGH Vector Core) to express palmitoylated tdTomato.

2.3. Cell culture

Wild-type and engineered MDA-MB-231 cells passed testing for mycoplasma contamination and were maintained in phenol-red-free DMEM (Corning) supplemented with 10% (v/v) fetal bovine serum (FBS), 100 units/ml penicillin, 100 μ g/ml streptomycin. Cells were cultured in a humidified atmosphere of 5% CO₂ at 37 °C. MDA-MB-436 cells harboring a BRCA1 5396 + 1G > A mutation also passed testing for mycoplasma contamination. The culture condition was same as that of MDA-MB-231 cells.

2.4. Mass spectrometry

Protein contents of MDA-MB-231 cells were detected by mass spectrometry (MS). After RIPA lysis, the protein amount in lysate was first determined via BCA protein assay (ThermoFisher, 23225). Samples were also processed for in-solution digestion and solid phase extraction. Label-free quantification was employed for the analysis. For database searching, all MS spectra were converted into DTA files. The protein-level FDR was also calculated and restricted to lower than 5%.

2.5. EV harvest and characterization

PD-L1^{KO}/havPD-1 MDA-MB-231 cells or PD-L1^{KO}/havPD-1/CD81-GFP MDA-MB-231 cells at 70% confluence were maintained with FBS-free medium for 24 h. The supernatant was collected and centrifuged at 20,000g for 15 min to discard cellular debris. Afterward, a total of 120 mL of supernatant was collected and ultracentrifuged at 100,000 g continuously at 4 °C for 2 h [26]. EV pellets were suspended in 200 μ l of PBS. Size distribution and concentration of EVs were measured with Nanosight NS300 according to manufacturer's instructions followed by automated analysis with NTA software. All EV samples were stored at -80 °C until use. 10 μ l diluted EV samples were loaded on 400-mesh Formvar-coated copper grids and allowed to incubate for 3 min at RT. Excess samples were drained with filter paper and stained with 1% filtered uranyl acetate solution of 3 min. The samples were observed by TEM at 200 kV. The amount of EV-derived proteins was determined using BCA protein Assay (ThermoFisher, 23225). Protein samples were analyzed with 12% sodium dodecyl sulfate-polyacrylamide gel electrophoresis, and then electrotransferred onto a nitrocellulose membrane. The membrane was blocked with 5% nonfat milk in PBS/0.05% Tween 20 for 30 min and washed thrice with DI water. Samples were incubated overnight at 4 °C with antibodies against PD-1 (Abcam, ab52587, 1:200), PD-L1 (Novus, NBP2-80490, 1:200), CD9 (Santa Cruz,

sc-13118, 1:500), CD47 (Abcam, ab175388, 1:500), CD55 (Abcam, ab96680, 1:500), CD59 (Abcam, ab133707, 1:500), TSG101 (Santa Cruz, sc-7964, 1:500), and GAPDH (Santa Cruz, sc-32233, 1:500). Afterward secondary antibodies were incubated for 1 h at RT. Samples were washed with PBS/0.05% Tween 20 for 10 min thrice. Blots were developed with chemiluminescence. A structured illumination microscope (Nikon, N-SIM) in super-resolution mode was used to visualize havPD-1/CD81-GFP EVs.

2.6. EV cell uptake

Approximately 8×10^5 havPD-1/CD81-GFP EVs were incubated with MDA-MB-231-tdTomato cells. The uptake was performed by incubating cell cultures with EVs for 10 min and 30 min at 37 °C. Cells were fixed with 4% paraformaldehyde at 4 °C for 10 min. Images of the cells were acquired using a 40 \times water immersion objective lens on Zeiss confocal microscope. In control group, PKH67 labeled wild-type MDA-MB-231 EVs expressing PD-L1 were incubated with MDA-MB-231-tdTomato cells. Detailed EV labeling procedure can be found elsewhere [27].

2.7. PD-L1 EV-havPD-1 EV binding

Wild-type MDA-MB-231 derived PD-L1 EVs and PD-L1^{KO}/havPD-1 MDA-MB-231 cells derived havPD-1 EVs were collected following the same procedure. Equal amount of PD-L1 EVs and havPD-1 EVs were thoroughly mixed and incubated at 37 °C for 2 h. Samples were observed under scanning electron microscope.

2.8. Estimation of havPD-1 amount on EVs

Approximately, 100 μ l of N-hydroxysulfosuccinimide (sulfo-NHS) and carbodiimide (EDC) (5:1, pH 5.0) were incubated with 20 μ g of anti-PD-1 antibody Fab fragment (Creative Biolabs, TAB-0961CL-F(E)) for 6 h at 37 °C to active carboxyl groups of antibody. At pH 7.2, 20 μ l of 0.1 mg/l monoamino Nanogold in 1.4 nm diameter (Nanoprobes, 2021S-6NMOL) were incubated with the mixture at 37 °C for 2 h to produce antibody Fab fragment grafted Nanogold [28]. The products were concentrated, filtered, resuspended in PBS, and stored at 4 °C. Subsequently, 1×10^7 havPD-1 EVs were incubated with 0.02 ng antibody functionalized Nanogold ($\sim 1 \times 10^{11}$ Nanogold) at 4 °C overnight followed by ultrafiltration with Amicon Ultracel-2 centrifugal filter (Millipore, UFC201024). The retrieved Nanogold-labeled havPD-1 EVs were resuspended in PBS and 5 μ l of samples were seeded onto poly-L-lysine coated silicon wafer and fixed in 4% paraformaldehyde for 3 h. Samples were lyophilized overnight followed by sputter-coating with gold at RT. The morphology of Nanogold-labeled havPD-1 EVs was shot under TEM. In an individual havPD-1 EV, the average Nanogold count and the corresponding surface area of havPD-1 EV were measured. Based on the calculated density of Nanogold and average diameter of havPD-1 EV, average havPD-1 count per EV was estimated.

2.9. Trypsin digestion of havPD-1 EVs and free havPD-1

Anti-PD-1 magnetic beads immunoprecipitation kit (SinoBiological, MB108583-T36) was used to harvest havPD-1 as per the manufacturer's instructions. In the other group, havPD-1 EVs were collected as previously described. The loading amount of free havPD-1 and havPD-1 EVs were tuned till similar intensity of PD-1 bands in western blot can be reached. Subsequently, optimized amount of free havPD-1 and havPD-1 EVs were digested with 10 ng/ μ l of trypsin (Promega, V5111) diluted in 505 mM NH₄HCO₃ at 37 °C for 30 min followed by supplement of fixation buffer (BD, 338036). The residual/loss of havPD-1 in respective group was semi-quantitatively analyzed with western blot and ImageJ. Moreover, after trypsin digestion havPD-1 EVs were labeled with anti-PD-1 antibody functionalized Nanogold following the established

protocol. The residual havPD-1 on EV membrane were visualized with TEM.

2.10. Surface plasmon resonance

Surface plasmon resonance (SPR, BIAcore X-100) was used to measure the binding kinetics of havPD-1 EVs to human PD-L1 at 37 °C. Recombinant hPD-L1-hFc proteins were immobilized on a CM5 chip using the Amine Coupling kit to get 1000 resonance units. 1 M Ethanolamine-HCL (pH 8.5) was used to deactivate remaining active esters. Approximately 1–1000 nM isolated and purified havPD-1 were injected into the microfluidic channel at a flow rate of 10 μ l/min. In control group, 1–1000 nM anti-PD-L1 Atezolizumab (BioVision) were injected over the antigen surface. The binding kinetics variables, including K_{on} , K_{off} , and K_D , were determined [29].

2.11. havPD-1 EV/PD-L1 blockade assay

PD-L1⁺ aAPC/CHO-K1 cells (Promega J1250) and PD-L1⁻ aAPC/CHO-K1 cells (Promega J1191) were plated in a 96-well tissue culture plate at $\sim 4 \times 10^4$ cells per well in 100 μ l of F-12 medium supplemented with 10% FBS, 0.2 mg/ml hygromycin and 0.2 mg/ml G418. The following day medium was removed. Serially diluted havPD-1 EVs and Atezolizumab were added at 40 μ l per well. Approximately 40 μ l of GloResponse NFAT-luc2/PD1 Jurkat cells (Promega, J1625) suspension at a concentration of 1.25×10^6 /ml were added to each well followed by co-culture for 6 h. Subsequently, Bio-Glo Reagent (Promega, G7940) was prepared as per the manufacturer's instructions and added to each well at 80 μ l per well. Plates were incubated for 5 min at RT followed by luminescence measurement using a plate reader. The IC₅₀ value was determined from the dose-response curves.

2.12. Mixed lymphocyte reaction

Fresh peripheral blood mononuclear cells (PBMC) derived from healthy volunteer donors were isolated with Ficoll-Paque Plus (GE Healthcare) as per the manufacturer's instructions. The Institutional Review Board approved the trial procedures, and informed consent was obtained in accordance with the Declaration of Helsinki. CD4⁺ T cells were isolated from PBMCs using Dynabeads untouched human CD4⁺ T cells kit (ThermoFisher, 11346D). Monocytes from another donor's PBMCs were used to generate dendritic cells (DC) by differentiation after incubation with 1000 IU/ml hGM-CSF and 1000 IU/ml hIL-4 for 5 days, followed by maturation in media containing 1000 U/ml Tumor necrosis factor alpha (TNF- α), 5 ng/ml IL-1 β , 10 ng/ml IL-6, and 1 μ M prostaglandin E2 (PGE₂) for 2 days. The two types of cells were then mixed in 96-well V-bottom plates with 1×10^4 DC and 1×10^5 CD4⁺ T cells. 100 μ l of 2 \times serially diluted havPD-1 EVs, Atezolizumab, or isotype control IgG1 was added. After incubation for 3 days at 37 °C and 5% CO₂, supernatants were harvested and subjected to detection of IFN γ with ELISA (R&D Systems, DIF50).

2.13. Recall antigen assay

Approximately 1×10^5 PBMCs per well were seeded in a 96-well tissue culture plate and cultured in 100 μ l of RPMI-1640 supplemented with 10% FBS overnight at 37 °C and 5% CO₂. havPD-1 EVs in various concentration were added to the cells at 50 μ l per well. In control group, 50 μ l of Atezolizumab or isotype control IgG1 were added. After 1-h incubation, 50 μ l of 0.8 μ g/ml Tetanus Toxoid (List labs, 191A) was added to wells. After 5-day culture, supernatant was collected and IFN γ was measured (R&D Systems, DIF50) according to manufacturer's instructions.

2.14. Antibody-dependent cellular cytotoxicity and complement-dependent cytotoxicity assays

The ability of havPD-1 EVs to mediate antibody-dependent cellular cytotoxicity (ADCC) was tested with 1×10^4 PD-L1⁺ HEL cells and Jurkat-Fc γ RIIIa (V158) cells. Cells were mixed together in assay medium and incubated at 37 °C and 5% CO₂ for 6 h under havPD-1 EVs, Atezolizumab, or ADCC-enhanced anti-PD-L1-hIgG1 antibody (InvivoGen, hpd11-mab13). Subsequently luciferase assay reagents were supplemented followed by detection of luminescence signal on a plate reader. Complement-dependent cytotoxicity (CDC) was tested with 1×10^4 PD-L1⁺ HEL cells in a well plate. Briefly, complement solution (Complementtech, A099) was added into wells and then incubated at 37 °C and 5% CO₂ for 2 h under havPD-1 EVs or Atezolizumab. Approximately 10 μ l of CCK-8 reagent (Dojindo) were added per well and incubated for 3 h. Cell viability was detected by measurement of the absorbance at 450 nm using a microplate reader.

2.15. Acute cytotoxicity assays for characterization of havPD-1 EVs

Approximately 3×10^5 MDA-MB-231 cells were treated with $\sim 8 \times 10^8$ havPD-1 EV, 300 ng/ml Atezolizumab or 300 ng/ml isotype IgG1. EdU cell proliferation assay (Sigma-aldrich, BCK-EDU488) was used to visualize cell proliferation according to manufacturer's instructions. To investigate cell migration, 2 well silicon insert (Ibidi, 80209) with a defined cell-free gap was attached on the bottom. 3×10^5 MDA-MB-231 cells were seeded into each well of a 24-well plate. When confluence reached 100%, silicon insert was removed. Cells were treated with $\sim 8 \times 10^8$ havPD-1 EV, 300 ng/ml Atezolizumab or 300 ng/ml isotype IgG1. The width of the wound was monitored under the microscope at 0, 6, 12, 18 and 24 h time points. ImageJ was used to calculate the wound area. The invasive potential of treated and untreated MDA-MB-231 cells was assessed with a tumor invasion system (Biocoat, Corning, 354167) following the manufacturer's instructions. Cells that had invaded through the Matrigel matrix membrane were stained with Wright-Giemsa for 15 min. The stained invasive cells were photographed and counted. In cell apoptosis assay, 5×10^6 MDA-MB-231 cells treated with $\sim 1 \times 10^{10}$ havPD-1 EVs, 300 ng/ml Atezolizumab, or 300 ng/ml isotype IgG1, respectively, in 100 μ l 1 \times binding buffer were incubated with 10 μ l of 20 μ g/ml 7-AAD and 5 μ l of 1 mg/ml Annexin V-FITC for 30 min at RT in the dark. Each sample was analyzed by Accuri-C6 flow cytometry. To visualize the cell apoptosis, cells were incubated with 2.5 mg/ml propidium iodide for 30 min at RT in the dark followed by analysis with a high-content imaging system.

2.16. RNA extraction and RT-qPCR

Total RNA was extracted from havPD-1 EV and Atezolizumab treated cells with Trizol reagent (ThermoFisher, 15596026) according to the manufacturer's protocol and quantified by Nanodrop. Subsequently, cDNA was synthesized with M-MLV reverse transcriptase kit (ThermoFisher, 28025013) according to the manufacturer's instructions. Sets of primers for β -ACTIN, PD-L1, NFKBIB, COMMD6, BTG2, RNF122, NBL1, ICAM3, and TRAF5 are shown in Table 1. PCR amplification was performed at 94 °C for 3 min, then 45 cycles at 94 °C for 1 min, 53 °C for 1 min and 72 °C for 1 min. Following amplification, the reactions were subjected to a thermal melt from 55 to 95 °C in 0.5 °C increments, and FAM fluorescence was monitored at each increment. Quantitative analysis of respective gene expression was determined with 2^{- $\Delta\Delta$ CT}, and normalized to β -ACTIN.

2.17. PARP1/2 inhibitor senaparib sensitivity assay

The treatment efficacy of PARP1/2 inhibitor Senaparib (IMPACT Therapeutics) against MDA-MB-436 cells was evaluated using CCK-8 assay. Approximately 4000 MDA-MB-436 cells were treated with

Table 1
| Primer sequence for the RT-qPCR.

	Primer sequence
<i>PD-L1</i>	F: 5'-TGG CAT TTG CTG AAC GCA TTT-3' R: 5'-TGC AGC CAG GTC TAA TTG TTT T-3'
<i>RNF122</i>	F: 5'-ATT CCA GTG GTG TAA CGG GTG-3' R: 5'-CCT GTG CCG AAG ATG ACC ATA-3'
<i>NBL1</i>	F: 5'-CAT GTG GGA GAT TGT GAC GCT-3' R: 5'-CCT CGT GAC TAG GCT CCT TG-3'
<i>ICAM3</i>	F: 5'-GGA GTT CCT TTT GCG GGT G-3' R: 5'-TCA GAG CTG GGA CAA TCA GTA-3'
<i>NFKB1B</i>	F: 5'-CGA CAC CTA CCT CGC TCA G-3' R: 5'-GTC GGA ATC GGG GTA CAA GG-3'
<i>TRAF5</i>	F: 5'-CCA CTC GGT GCT TCA CAA C-3' R: 5'-GTA CCG GCC CAG AAT AAC CT-3'
<i>β-ACTIN</i>	F: 5'-AGA GCT ACG AGC TGC CTG AC-3' R: 5'-AGC ACT GTG TTG GCG TAC AG-3'

Senaparib and Olaparib (AstraZeneca) in various concentrations, ranging from 0 to 10000 nM. The IC₅₀ was determined from the dose-response curves.

2.18. Senaparib loading and release

Senaparib and havPD-1 EVs were mixed in number ratio of 10⁵. Senaparib was loaded into havPD-1 EVs with sonication. The experimental details can be found elsewhere [10]. Excess free Senaparib was removed with a Sephadex G25 column. The amount of loaded Senaparib was measured by HPLC. To measure Senaparib release, freshly prepared Senaparib-loaded havPD-1 EVs was placed in a 300K MWCO float-A-lyzer G2 device (Spectrum Laboratories). The device was then placed in PBS at RT with stirring. Samples were taken at timepoints and analyzed by HPLC.

2.19. Therapeutic efficacy of havPD-1 EVs in co-implantation model and xenograft model

All animal experiments were approved by and performed in accordance with guidelines from the Institutional Animal Care and Use Committee (IACUC) of the Model Animal Research Center of the Wuxi People's Hospital Affiliated to Nanjing Medical University (Wuxi, Jiangsu, China). Freshly isolated 1 × 10⁶ human PBMCs were combined with 5 × 10⁶ MDA-MB-231 cells at a 1:5 E:T ratio and co-implanted subcutaneously to the flanks of NOD-SCID MICE (18–22 g, 4–6 weeks, 5 mice per group). Intraperitoneal injection (*i.p.*) of 2 × 10¹³/kg havPD-1 EVs were performed twice a week [30]. In control groups, 3.3 mg/kg Atezolizumab or 3.3 mg/kg isotype control IgG1 were administered *i.p.* for a total of 4 doses. Tumor volume was monitored by caliper measurements. Approximately 5 × 10⁶ MDA-MB-231 cells were inoculated subcutaneously to the flanks of NOD-SCID mice and allowed to grow to a tumor size approximately 200 mm³. Approximately 1 × 10⁶ human T cells were intravenously administered, and mice were intraperitoneally treated with 6 × 10¹³/kg havPD-1 EVs, 10 mg/kg Atezolizumab, or 10 mg/kg isotype control IgG1 for a total of four doses. Tumor volume was monitored by caliper measurements. Mice were euthanized to harvest tumors.

2.20. Therapeutic efficacy of senaparib loaded havPD-1 EVs in xenograft model

Approximately 5 × 10⁶ MDA-MB-436 cells were inoculated subcutaneously to the flanks of NOD-SCID mice and allowed to grow to a tumor size approximately 200 mm³. Approximately 1 × 10⁶ human T cells were intravenously administered, and mice were intravenously treated with PBS, 2 mg/kg Senaparib, 6 mg/kg Senaparib, 6 × 10¹³/kg havPD-1 EVs, 2 mg/kg Senaparib and 6 × 10¹³/kg havPD-1 EVs, and 2 mg/kg Senaparib loaded havPD-1 EVs (additional havPD-1 EVs without

Senaparib loading were supplied to ensure the final concentration of havPD-1 EVs was 6 × 10¹³/kg). Drug was intraperitoneally administered twice a week for 3 weeks. Tumor volume was monitored by caliper measurements. Mice were euthanized to harvest tumors. To study pharmacokinetics of Senaparib, 0.1–0.3 g tumor tissue samples were collected at 0.5, 1, 3, 6, 12, and 24 time points after intraperitoneal administration of free Senaparib or Senaparib-loaded havPD-1 EVs. The analysis of Senaparib by HPLC followed the published protocol [31]. In parallel, to visualize havPD-1/CD81-GFP EVs in blood circulation retro-orbital blood was collected at 1-h time point after intraperitoneal administration. Images were acquired using a confocal microscope. In xenograft model of BRCA wild-type MDA-MB-231 cells, ~5 × 10⁶ MDA-MB-231 cells were inoculated subcutaneously to the flanks of NOD-SCID mice and allowed to grow to a tumor size approximately 200 mm³. Approximately 1 × 10⁶ human T cells were intravenously administered, and mice were intravenously treated with PBS, 6 mg/kg Senaparib, 6 × 10¹³/kg havPD-1 EVs, and 6 mg/kg Senaparib loaded havPD-1 EVs. Drug was intraperitoneally administered twice a week for 3 weeks. Tumor volume was monitored by caliper measurements. Mice were euthanized to harvest tumors.

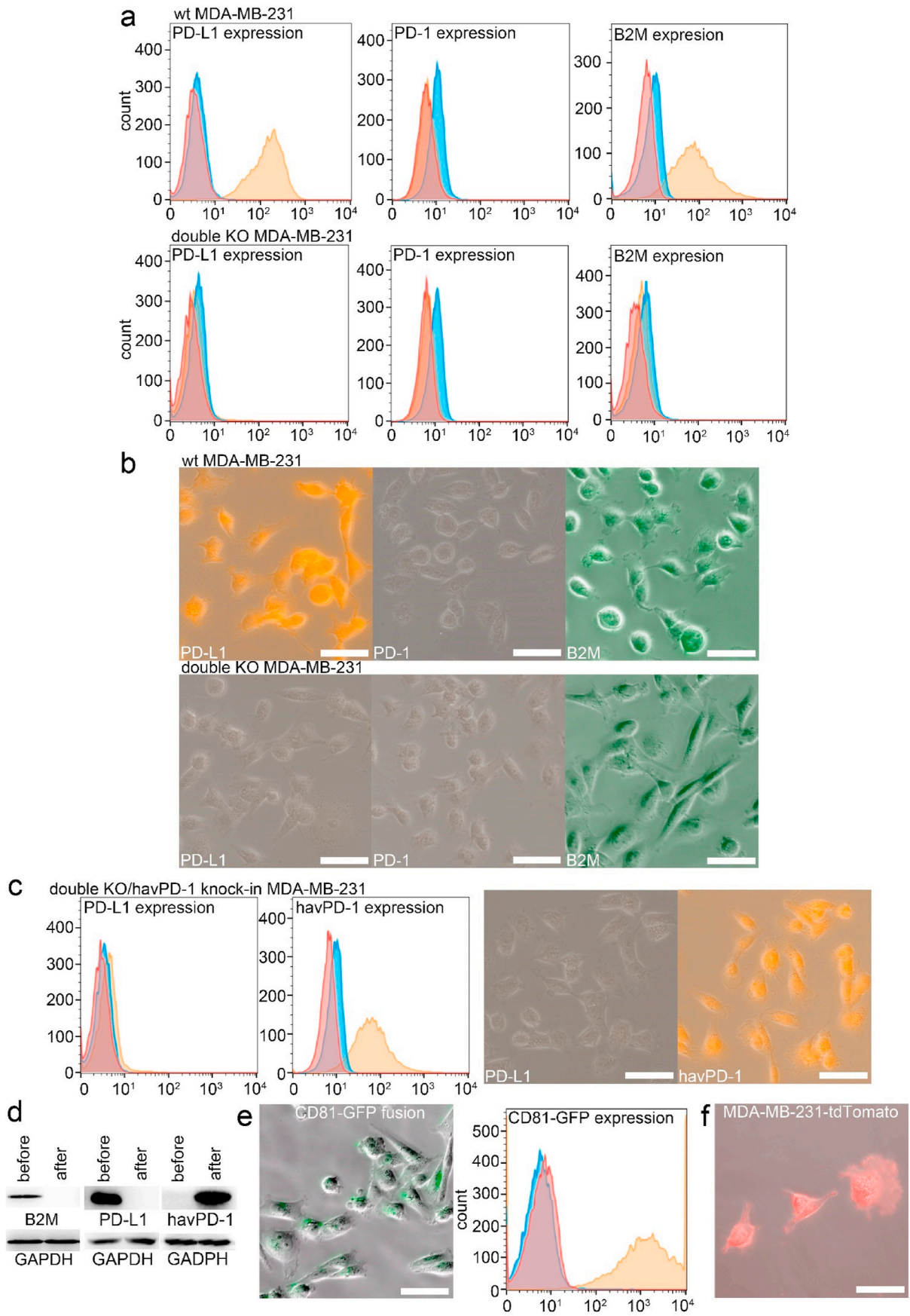
2.21. Statistical analyses

Results are presented as mean ± SD. Statistical comparisons were performed by paired Student *t*-test or ANOVA.

3. Results

Cell construction. To generate double-KO MDA-MB-231 cells lacking PD-L1 and HLA-I, Cas9 mRNA was co-electroporated with two different gRNAs targeting PD-L1 exon 3 and beta-2 microglobulin (B2M) exon 1 (B2M is essential for the assembly and expression of the HLA-I complex). Single cells from the generated cell pool were then seeded into wells of a 384 well plate. These wells were imaged for colony outgrowth of surviving transfectants and confirmation of clonality. Homozygous knockouts were confirmed by Sanger sequencing (Supplementary Fig. 1). A clone which lacked both PD-L1 and HLA-1 was selected for further use. Flow cytometry and immunofluorescence staining confirmed the successful KO of B2M and PD-L1 (Fig. 2a and b). Subsequently, the previously reported havPD-1 was overexpressed in this B2M/PD-L1 double deficient MDA-MB-231 cell line (Fig. 2c) [24]. Western blot further confirmed the expression of PD-L1, PD-1, and B2M (Fig. 2d). It is noteworthy that to avoid a potential cellular abnormality, we expressed only the extracellular and transmembrane domains of havPD-1. Without the intact cytoplasmic domain, the PD-1/PD-L1 interaction will not trigger the intracellular-signaling transduction and cellular response [32]. The havPD-1 overexpressing MDA-MB-231 cells were labeled with fluorescent anti-PD-1 antibody followed by sorting. The quantitative flow cytometry determined that average ~7.1 × 10⁴ intrinsic PD-L1 molecules on wild-type MDA-MB-231 cells were knocked out and average ~2.8 × 10⁴ havPD-1 molecules were expressed on the constructed MDA-MB-231 cells. To facilitate visualization and tracking of derived havPD-1 EVs, CD81-GFP fusion was further knocked-in (Fig. 2e). After sorting, over 99.8% of stably transfected double-KO/havPD-1 knock-in MDA-MB-231 cells express CD81-GFP fusion proteins. Furthermore, we generated wild-type MDA-MB-231 cells that bear an intrinsic palmitoylated tdTomato which can be spontaneously integrated into the plasma membrane via the lipid tail (Fig. 2f). Approximately 92.1% of the cells stably express palmitoylated tdTomato proteins.

EV characterization. havPD-1 EVs were harvested from cell culture supernatant by ultracentrifugation. The average size of havPD-1 EVs was 112.7 nm (Fig. 3a). To demonstrate that the EV lipid envelop can retard the cleavage of havPD-1 on EVs by limiting the access of proteases, havPD-1 EVs and bare havPD-1 proteins were incubated with trypsin. The western blot demonstrated bare havPD-1 proteins were completely



(caption on next page)

Fig. 2. Characterization of constructed cells. (a) The expression level of PD-L1, PD-1, and B2M as measured by flow cytometry in wild-type MDA-MB-231 and double-KO MDA-MB-231 (Red: blank; Blue: Isotype antibody; Yellow: anti-PD-L1, anti-PD-1, or anti-B2M antibody). (b) Fluorescent image of PD-L1, PD-1, and B2M in wild-type and double-KO MDA-MB-231 cells (scale bar is 10 μm). (c) The expression level of PD-L1 and havPD-1 as measured by flow cytometry and fluorescence microscopy in double-KO/havPD-1 knock-in MDA-MB-231 cells (Red: blank; Blue: Isotype antibody; Yellow: anti-PD-L1 or anti-PD-1 antibody; scale bar is 10 μm). (d) B2M, PD-L1, and havPD-1 proteins were extracted and identified from wild-type and constructed MDA-MB-231 cells. (e) Fluorescent image of constructed double-KO/havPD-1 knock-in/CD81-GFP fusion MDA-MB-231 cells (scale bar is 10 μm) and the expression level of CD81-GFP as measured by flow cytometry (Red: blank; Blue: MDA-MB-231 cells w/o CD81-GFP fusion protein; Yellow: MDA-MB-231 cells expressing CD81-GFP fusion protein). (f) Fluorescent image of constructed MDA-MB-231-tdTomato cells (scale bar is 10 μm).

degraded. In contrast, partial havPD-1 proteins on EVs still were detectable from treated havPD-1 EVs (Fig. 3b), and the signal intensity of havPD-1 decreased to $\sim 36.9\%$. Subsequently, we used anti-PD-1 Fab-conjugated immunogold nanoparticle which contains only one antigen combining region to estimate the amount of havPD-1 molecules on EVs (Fig. 3c). Average 19 immunogold nanoparticles were identified by *ImageJ* ($n = 214$). The immunogold staining further demonstrated the surviving havPD-1 EVs after trypsin treatment and the remaining havPD-1 proteins on membranes (Fig. 3c). The average amount of havPD-1 on surviving EVs also decreased to 12 havPD-1 proteins per EV ($n = 53$). Moreover, western blot revealed havPD-1 EVs harbor classic EV markers TSG101, CD9, and housekeeping protein GAPDH. Membrane antigens, including CD47, CD55, and CD59 were also detectable (Fig. 3d), indicating these EVs can inhibit phagocytosis and restrain the activation of complement. Next, we measured the binding affinity of the havPD-1 with PD-L1. The affinity of this engineered havPD-1 is ~ 110 pM, and dissociation half-life is ~ 40 min [24]. The surface plasmon resonance analysis determined the K_d of truncated havPD-1 proteins on EV membrane is ~ 102 pM which is very close to the reported value [24]. In contrast, the K_d of commercial anti-PD-L1 mAb, Atezolizumab, was determined to be 197 pM which also falls within the reported range (Fig. 3e) [33]. The specificity of havPD-1 was validated in the previous study [24]. Therefore, we did not further assess the potential binding of havPD-1 to other human B7 family proteins or mouse PD-L1. We harvested wild-type MDA-MB-231 derived PD-L1 overexpressing EVs (Fig. 3f) and mixed them with havPD-1 EVs in a 1:1 ratio. Unsurprisingly, macroscopic agglomeration quickly developed in less than 10 min (Fig. 3g). Recent studies revealed circulating PD-L1 expressing EVs can inhibit the anti-tumor activities of T cells by binding to its receptor PD-1 [34,35]. Therefore, cancer treatment would benefit from therapeutics that block PD-L1 expressing EV production, and removal of circulating PD-L1 expressing EVs would improve immunotherapy efficacy and attenuate oncogenic EV-induced cancer metastasis [36–38]. We hypothesized that our havPD-1 EVs may function to neutralize tumor derived PD-L1 EVs, and the resulting agglomeration would enhance macrophage phagocytosis thus leading to PD-L1 EV clearance.

To track EVs, we harvested havPD-1/GFP EVs. The average size of havPD-1/GFP EVs was 113.4 nm. Compared to havPD-1 EV, no significant difference in size was found between the two (two-tailed *t*-test, $p > 0.05$). Both exhibited the characteristic saucer-shaped morphology under electron microscopy (Fig. 3a and h). In addition, havPD-1/GFP EVs were directly observed with a super-resolution microscopy in SIM mode (Fig. 3h). The average size of havPD-1/GFP EVs measured by microscopy ranged from 110 to 450 nm. Given the lateral resolution of SIM mode is 85–115 nm, small havPD-1/GFP EVs therefore were unable to be observed. Next, we performed a cell binding assay that demonstrated that havPD-1/GFP EVs efficiently bound PD-L1 overexpressing MDA-MB-231-tdTomato cells in only 10 min (Fig. 3i). In contrast, equal amount of PKH67-labeled PD-L1 expressing EVs derived from wild-type MDA-MB-231 cells exhibited negligible fusion with MDA-MB-231-tdTomato cells at the same time point. After 30 min, a few PKH67-labeled PD-L1 expressing EVs fused with cell membrane, while significant amount of havPD-1/GFP EVs were observed in the experimental group (two-tailed *t*-test, $p < 0.01$). The findings indicate that havPD-1 EVs can rapidly recognize and bind onto PD-L1 expressing cancer cell surface, and thus can block PD-L1 and facilitate drug delivery targeting PD-L1.

Biological effects of havPD-1 EVs on cancer cells. The engineered double-KO/havPD-1 knock-in MDA-MB-231 cells demonstrated low proliferation rate, exhibiting a doubling time of ~ 43.5 h. In contrast, the doubling time of wild-type MDA-MB-231 is ~ 18.8 h. We also observed the KO of PD-L1 increased apoptosis in the engineered MDA-MB-231 cells, which is in line with findings reported in previously studies [39, 40]. Similarly, PD-L1 blockade by mAbs is known to inhibit cancer cell proliferation, migration, and invasion [41,42]. Based on this, we speculated the double-KO/havPD-1 knock-in MDA-MB-231 cells derived havPD-1 EVs may have similar effects. Confirming this hypothesis, we performed a wound-healing assay and demonstrated that the wound-closure rate of wild-type MDA-MB-231 cells is ~ 7.7 -fold slower after havPD-1 EV treatment (ANOVA, $p < 0.01$), in comparison with a PBS treated control (Fig. 4a and b). By comparison, Atezolizumab treatment resulted in a ~ 6.7 -fold reduction in the wound-closure rate. No significant difference in wound size was found between havPD-1 EV group and Atezolizumab group (ANOVA, $p > 0.05$). Similarly, a transwell invasion assay showed the invasion of wild-type MDA-MB-231 cells treated with either havPD-1 EVs or Atezolizumab was ~ 8 -fold decreased over controls (ANOVA, $p < 0.01$, Fig. 4c). Moreover, an EdU assay demonstrated the division percentage of wild-type MDA-MB-231 cells in havPD-1 EV group and Atezolizumab group was ~ 2.5 -fold and ~ 1.9 -fold less, respectively, than that of negative controls (ANOVA, $p < 0.05$, Fig. 4d and e). Cell apoptosis occurring following treatment with havPD-1 EVs and Atezolizumab, respectively, were investigated by flow cytometry. In havPD-1 EV group, the percentage of apoptotic cells was increased ~ 10 -fold over the negative control (Fig. 4f). In comparison, Atezolizumab also increased the percentage of apoptotic cells by a similar amount (~ 7 -fold). The high-content screening confirmed significantly more apoptotic cells (stained in red) in groups treated with havPD-1 EVs and Atezolizumab in comparison with that of negative controls (Fig. 4g). Following the reported mRNA profile of Atezolizumab treated breast cancer cells [41], we selected 6 genes for PCR validation. Both havPD-1 EVs and Atezolizumab upregulated mRNA expression of *RNF122*, *NBL1*, and *NFKB1B* (Fig. 4h). The fold change ranges from 1.4 to 1.7 (ANOVA, $p < 0.05$). These genes are associated with pro-apoptosis, tumor suppression, and DNA repair, respectively [41]. On the contrary, *ICAM3* promoting cell migration, invasion, and metastasis was downregulated by ~ 3 -fold (ANOVA, $p < 0.05$). Of note, neither havPD-1 EVs nor Atezolizumab altered *PD-L1* mRNA expression (ANOVA, $p > 0.05$).

Anticancer immune response of havPD-1 in vitro. We utilized a PD-L1 neutralization reporter assay to identify whether havPD-1 EVs can neutralize PD-L1 on cell membranes. Addition of havPD-1 resulted in a concentration-dependent increase in NFAT-driven expression of luciferase, which overcame the inhibitory effects of PD-L1 expressed by CHO cells (Fig. 5a). Based on the depicted dose-response curve, we determined IC_{50} of havPD-1 EVs was 2.1×10^{10} EV/ml compared to 223 pM for Atezolizumab. In mixed leukocyte reactions (MLR), addition of havPD-1 EVs enhanced T cell response (as assessed by IFN- γ production) in a dose-dependent manner, with activity observed at concentrations as low as $\sim 2 \times 10^7$ EV/ml compared to ~ 15 pM for Atezolizumab (Fig. 5b). Moreover, both havPD-1 EVs and Atezolizumab were shown to enhance T cell activity in the tetanus-toxoid recall assay which measures the ability to stimulate antigen-specific memory T cells in human peripheral blood mononuclear cells (PBMC, Fig. 5c). Next, we investigated whether havPD-1 EVs can induce antibody-dependent cellular cytotoxicity

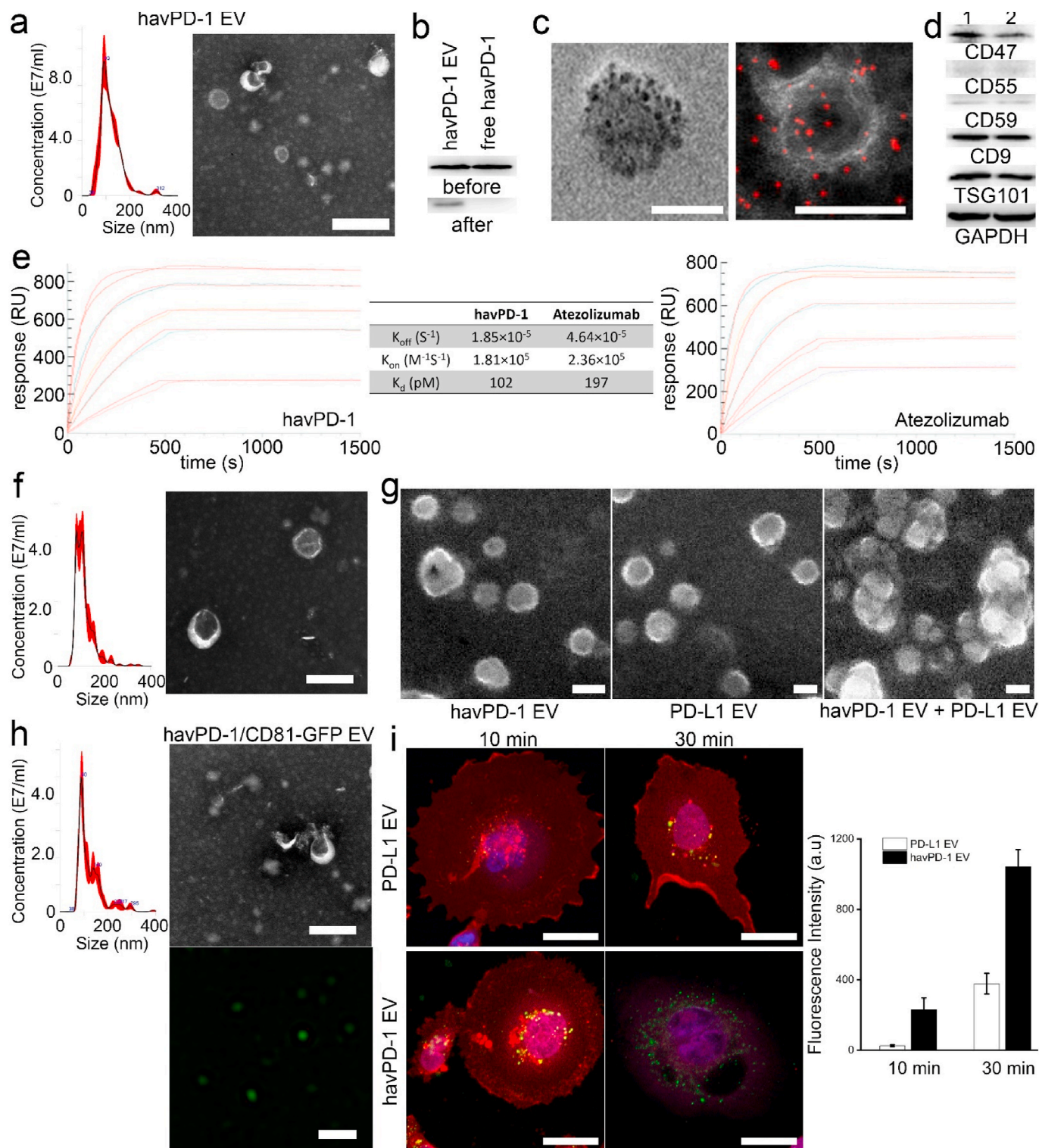
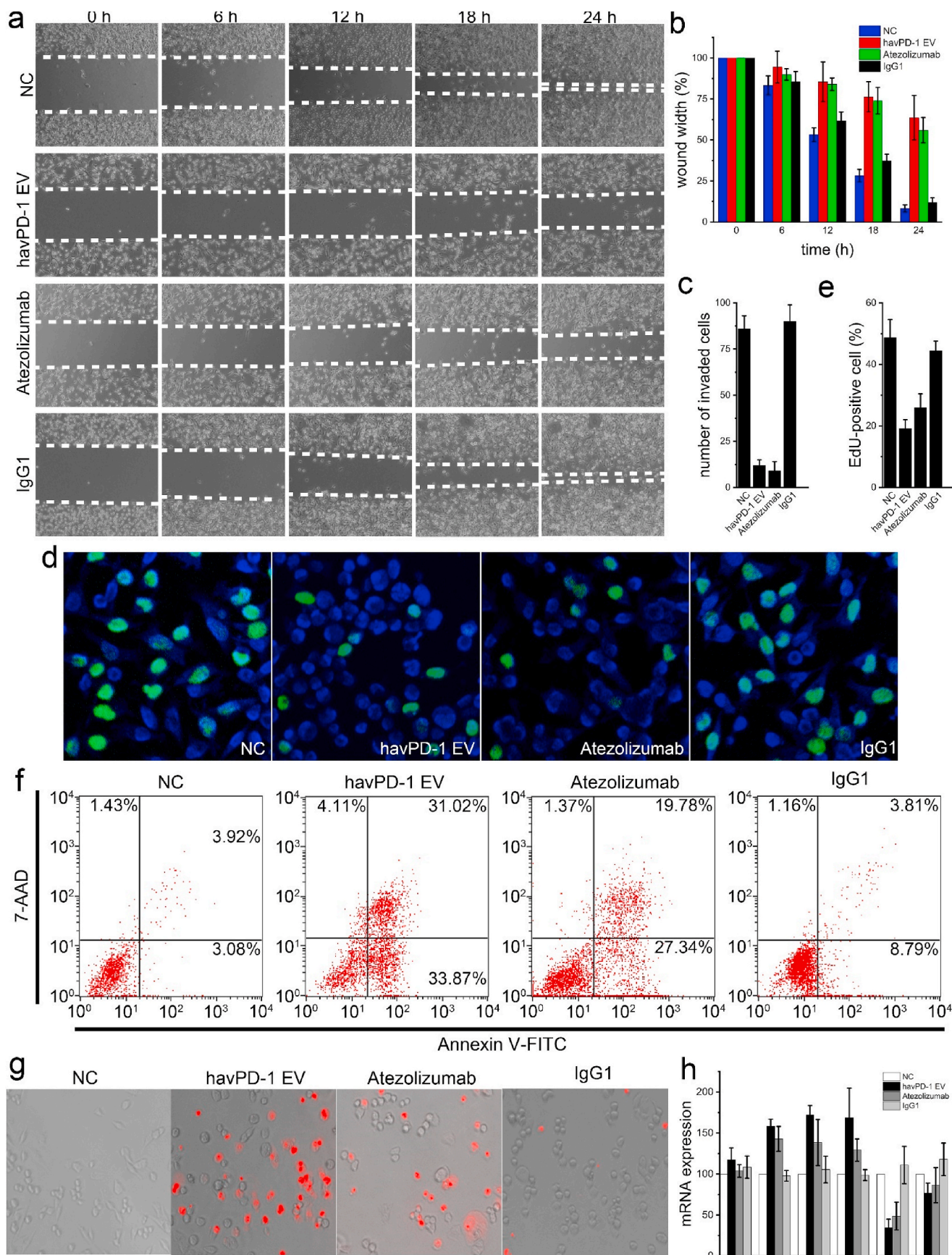


Fig. 3. Characterization of EVs. (a) Size distribution of havPD-1 EVs (left) and morphology characterization of havPD-1 EVs by electron microscopy (scale bar is 100 nm). (b) Western blot analysis of havPD-1 extracted from trypsin-treated havPD-1 EVs and free havPD-1. (c) TEM image of havPD-1 EVs stained with anti-PD-1 antibodies grafted gold nanoparticle (scale bar is 50 nm) and STEM image of surviving havPD-1 EVs stained with immunogold (red dots; scale bar is 100 nm). (d) Western blot analysis of CD47, CD55, CD59, CD9, TSG101, and GAPDH extracted from havPD-1 EVs (1) and havPD-1/GFP EVs (2). (e) Association and dissociation of havPD-1 or Atezolizumab to PD-L1 by SPR. (f) Size distribution of PD-L1 EVs (left) and morphology characterization of PD-L1 EVs by electron microscopy (scale bar is 100 nm). (g) Morphology of havPD-1 EVs, PD-L1 EVs, and their mixture (scale bar is 100 nm). (h) Size distribution of havPD-1/CD81-GFP EVs (left); morphology characterization of havPD-1/CD81-GFP EVs by electron microscopy (middle, scale bar is 100 nm); Fluorescence image of havPD-1/CD81-GFP EVs (right, scale bar is 1 μ m). (i) Fluorescence images and quantified data of fluorescence intensity of each group (n = 15) showing PKH67-labeled PD-L1 EVs and havPD-1/GFP EVs taken up by MDA-MB-231-tdTomato cells in 30 min (scale bar is 10 μ m).



(caption on next page)

Fig. 4. Cell migration, invasion, proliferation, and apoptosis. (a) Wound healing assay of MDA-MB-231 cells treated with PBS, havPD-1 EVs, Atezolizumab, and isotype IgG1, respectively. Migration was assessed at 6, 12, 18, and 24 h time points after wounding, respectively. (b) Quantification of wound closure showing havPD-1 EV and Atezolizumab inhibited migration of MDA-MB-231 cells compared to the controls ($n = 6$, $p < 0.01$, ANOVA). (c) Quantification of the invasion assay showing havPD-1 EV and Atezolizumab inhibited invasion of MDA-MB-231 cells compared to the controls ($n = 5$, $p < 0.01$, ANOVA). (d) Fluorescence images showing dividing MDA-MB-231 cells treated in each group (green: Edu staining; blue: DAPI staining). (e) Quantification of proportion of dividing cells in each group showing havPD-1 EV and Atezolizumab inhibited proliferation of MDA-MB-231 cells ($n = 3$, $p < 0.05$, ANOVA). (f) Apoptotic status of MDA-MB-231 cells in each group. (g) Fluorescence images of MDA-MB-231 cells treated with PBS, havPD-1 EVs, Atezolizumab, isotype IgG1 in each group followed by propidium iodide staining. (h) RT-qPCR analysis of selected gene expression of MDA-MB-231 cells in each group ($n = 3$).

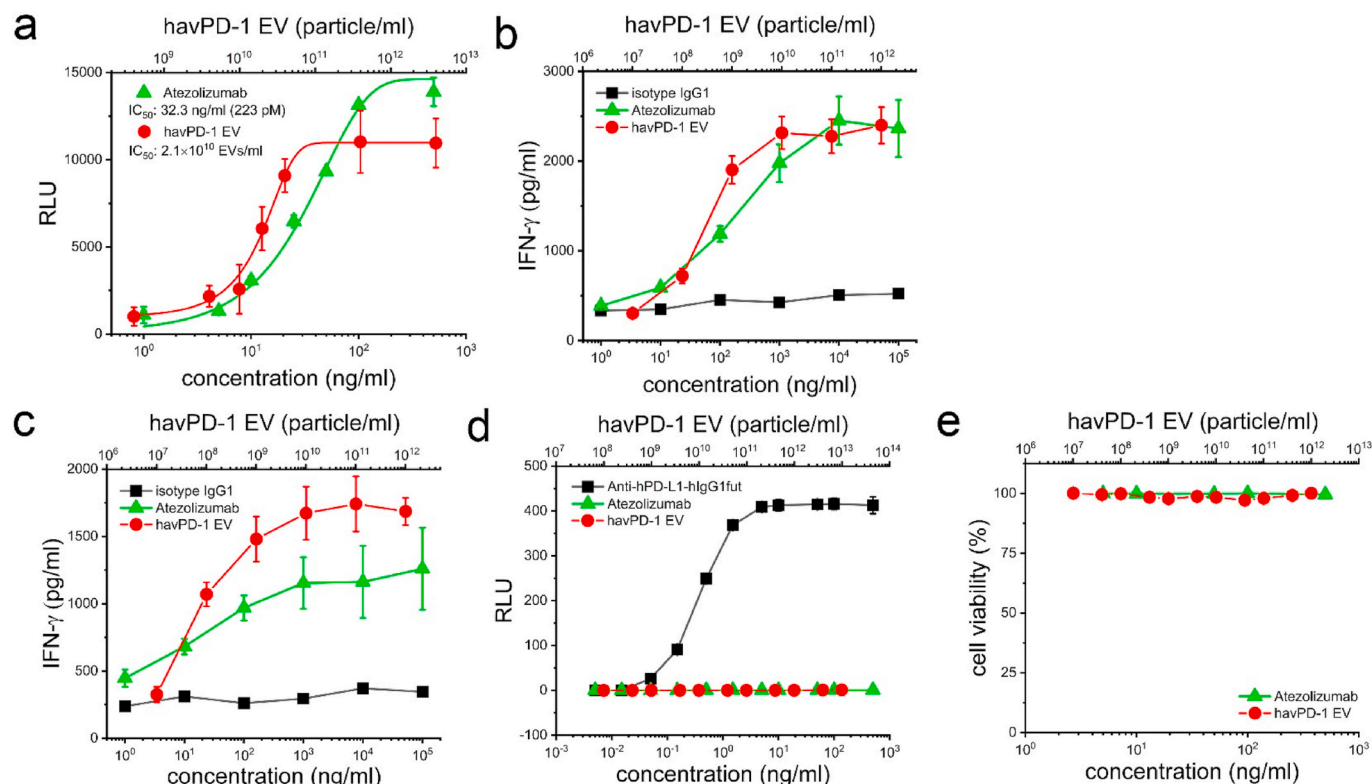


Fig. 5. Functional activity of havPD-1 EVs in cell-based assays. (a) Neutralization of PD-L1 in a cell assay by havPD-1 EVs in comparison with a clinical control, Atezolizumab. (b) Mixed lymphocyte reaction assay. Supernatants were measured for IFN- γ production by ELISA ($n = 8$). (c) Tetanus toxoids recall assay. Supernatants were measured for IFN- γ production by ELISA ($n = 8$). (d) Antigen-dependent cell-mediated cytotoxicity assay ($n = 8$). (e) Complement dependent cytotoxicity assay ($n = 8$).

(ADCC) and complement-dependent cytotoxicity (CDC). Atezolizumab is engineered to ablate Fc-gamma receptor engagement. Therefore, Atezolizumab did not direct detectable effector function activity against target cells. No significant response was observed in havPD-1 EVs either. On the contrary, ADCC-enhanced anti-PD-L1-hIgG1fut antibody was shown to mediate significant ADCC response (Fig. 5d). Moreover, neither havPD-1 nor EVs and Atezolizumab significantly triggered CDC (Fig. 5e).

Monotherapy using havPD-1 EVs *in vivo*. Biological activity of havPD-1 EVs *in vivo* was evaluated using two mice models. In co-implantation model, mice were co-implanted with a mixture of human PBMCs and wild-type MDA-MB-231 cells, followed by administration of havPD-1 EVs or controls. Intraperitoneal injection (*i.p.*) of 2×10^{13} /kg havPD-1 EVs were performed twice a week. In control groups, 3.3 mg/kg Atezolizumab or 3.3 mg/kg isotype control IgG1 were administered *i.p.* for a total of 4 doses. Both havPD-1 EVs and Atezolizumab significantly inhibited tumor growth (ANOVA, $p < 0.01$). In contrast, the average tumor volume in two negative controls had a ~ 12 -fold larger size compared with two experimental groups at the end timepoint (Fig. 6a). In a xenograft model, administration of havPD-1 EVs and Atezolizumab efficiently inhibited tumor growth. Tumor volume was ~ 4 -fold smaller than that of negative controls, reflecting both enhanced anti-tumor

reactivity of the engrafted T cells (Fig. 6b).

Preparation and characterization of Senaparib-loaded havPD-1 EVs. In order to further expand the utility of the havPD-1 EVs, we undertook the preparation and evaluation of drug-loaded havPD-1 EVs. PARP inhibitors are well-studied anti-tumor agents that block DNA repair, resulting in synthetic lethality. We selected Senaparib (IMP4297) (IC_{50} : ~ 5.2 nM in MDA-MB-436 cells) for incorporation into the EVs based on its exceptional potency and ready availability (Supplementary Fig. 2a) [43,44]. The average loading efficiency of Senaparib upon sonication with the EV was 29.8%. After Senaparib loading, the average size of havPD-1 EVs slightly increased from 111.2 nm to 117.4 nm (Supplementary Fig. 2b). The mean zeta potential of havPD-1 EVs increased from -10.8 mv to -7.1 mv (Supplementary Fig. 2c), indicating the weakly basic Senaparib was loaded into havPD-1 EVs. Under electron microscopy, there was no significant difference in morphology between havPD-1 EVs and Senaparib-loaded havPD-1 EVs (Supplementary Fig. 2d). The release kinetics of Senaparib from havPD-1 EVs at 37°C was determined by HPLC (Supplementary Fig. 2e). Hydrophobic Senaparib slowly diffused out of havPD-1 EVs and displayed a sustained release profile over 48 h. At 48-h time point, $\sim 23.3\%$ loaded Senaparib was released from havPD-1 EVs. The EVs could be cryopreserved batches for ~ 6 months and then thawed for use [10].

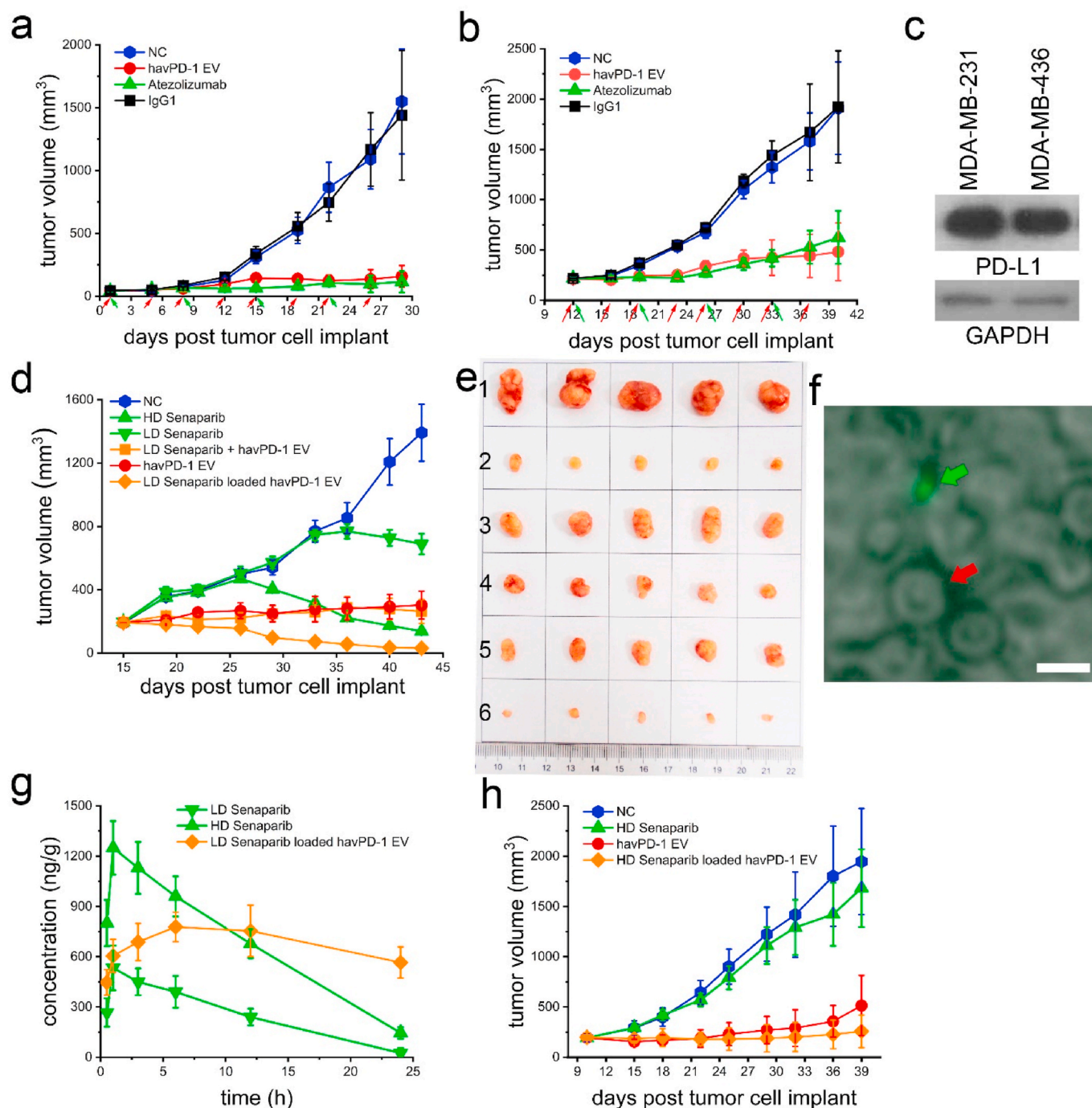


Fig. 6. Tumor treatment *in vivo*. (a) Co-implantation model: tumor volume of MDA-MB-231 tumor in mice from each group after drug or placebo administration (n = 5). (b) Xenograft model: tumor volume of MDA-MB-231 tumor in mice from each group after drug or placebo administration (n = 3). (c) PD-L1 proteins were extracted and identified from MDA-MB-231 cells and MDA-MB436 cells, respectively, by western blot. (d) Xenograft model: tumor volume of MDA-MB-436 tumor in mice from each group after drug or placebo administration (n = 5). (e) MDA-MB-436 tumor tissues obtained from each group of euthanized mice (n = 5) after administration of PBS (1), 6 mg/kg Senaparib (2), 2 mg/kg Senaparib (3), 2 mg/kg Senaparib and 6×10^{13} /kg havPD-1 EVs (4), 6×10^{13} /kg havPD-1 EVs (5), and 2 mg/kg Senaparib loaded havPD-1 EVs (6). (f) Identification of havPD-1/GFP EVs in peripheral blood at 1-h time point after intraperitoneally administration (scale bar is 5 μ m). A red blood cell and a havPD-1 EVs are indicated by white arrows. (g) Respective pharmacokinetics of Senaparib in plasma. (h) Xenograft model: tumor volume of MDA-MB-231 tumor in mice from each group after drug or placebo administration (n = 3).

Combination therapy using Senaparib-loaded havPD-1 EVs *in vivo*. Having prepared the appropriate Senaparib-loaded havPD-1 EVs, we proceeded to investigate the treatment efficacy in a xenograft model of BRCA1-mutant MDA-MB-436 cells. The PD-L1 expression level in MDA-MB-436 was analyzed with western blot (Fig. 6c). Compared to MDA-MB-231 cells, PD-L1 expression was ~31% lower in MDA-MB-436 cells. In animal study, we judiciously chose 2 mg/kg (low-dose, LD) and

6 mg/kg (high-dose, HD) Senaparib to treat an MDA-MB-436 xenograft mouse model. After administration of free Senaparib, tumor volume in HD group decreased significantly to ~140 mm³ at endpoint compared to ~690 mm³ for LD, indicating the cytostatic efficacy of LD Senaparib was inefficient (Fig. 6d and e). The mixture of havPD-1 EVs and LD Senaparib significantly inhibited tumor growth. Tumor volume at the endpoint was ~260 mm³. Of note, havPD-1 EVs contributed significantly to the

inhibitory effect as tumor treated with havPD-1 EV alone increased to only $\sim 300 \text{ mm}^3$. In contrast, LD Senaparib loaded havPD-1 EVs decreased the tumor volume to $\sim 30 \text{ mm}^3$, indicating LD Senaparib was efficiently delivered to cytosol of MDA-MB-436 cells via havPD-1 EVs. In addition, we investigated the pharmacokinetics (PK) of Senaparib in blood. Fluorescence images showed the Senaparib loaded havPD-1/GFP EVs entered in blood circulation after 1-h intraperitoneal injection (Fig. 6f). At 1 h post administration, peak plasma concentration of Senaparib occurred in LD and HD groups, and then plasma concentration of Senaparib in these two groups steadily decreased in the next 24 h (Fig. 6g). In LD Senaparib-loaded havPD-1 EV group, peak plasma concentration occurred at 6 h post administration and slowly decreased in the next 18 h. At the 24-h time point, Senaparib concentration in peripheral blood was significantly higher than that in free Senaparib groups (ANOVA, $p < 0.05$), indicating encapsulation of Senaparib into havPD-1 EVs can change PK of Senaparib likely due to reduced renal clearance. Long circulation time of havPD-1 EVs and target-specific delivery of Senaparib in combination with havPD-1 mediated PD-L1 blockade, therefore, can potentially improve treatment efficacy. Finally, we tested the therapeutic effect of HD Senaparib-loaded havPD-1 EVs in a xenograft model of BRCA wild-type MDA-MB-231 cells. No significant difference in tumor volume was observed between negative control and free HD Senaparib treated group (ANOVA, $p > 0.05$), indicating low efficiency of Senaparib in BRCA wild-type models (Fig. 6h). At the end timepoint, average tumor volume in free HD Senaparib and HD Senaparib-loaded havPD-1 EVs groups was 514 mm^3 and 258 mm^3 , respectively. The difference in tumor volume was very close to being statistically significant (ANOVA, $p > 0.05$). Nevertheless, the combination therapy efficiently inhibited tumor growth over the 28-day treatment.

4. Discussion

Triple-negative breast cancers (TNBC) lack human epidermal growth factor receptors 2 (HER2), estrogen receptors, and progesterone receptors [45]. Current drugs and treatment regimens have limited efficacy against TNBC due to the lack of specific targets and poor durability of chemotherapeutic responses [46], partially accounting for the high relapse rates. Meanwhile, PD-L1 is expressed in $\sim 20\%$ of TNBCs [47], which allows them to escape immune recognition even though there is an abundance of stromal and intratumoral lymphocytes frequently observed in TNBCs [48]. Therefore, new therapeutic approaches for TNBCs are of significant interest. There have been several recent reports of phase I and II clinical trials testing combination therapies of ICI and small-molecule chemotherapeutics against TNBC [49]. Together, the challenges in treating TNBCs and shortcomings of ICI mAbs impelled us to develop EV-based concurrent immunotherapy and chemotherapy.

In order to facilitate the investigation of EVs that targeting immune checkpoints, PD-L1 overexpressing tumor cells are preferred to PD-L1-deficient tumor cells [50]. Therefore, we deliberately chose PD-L1 overexpressing MDA-MB-231 cells, a commonly used TNBC cell line, as donor cells for construction of EVs and as targets to validate the function of our engineered EVs. An additional benefit of construction of MDA-MB-231 cells is that the derived EVs naturally possess a breast tumor-homing effect, which may mitigate on-target off-tumor toxicity. Moreover, protein sequencing data reveals that MDA-MB-231 cell express CD47, CD55, and CD59 antigens (supplementary dataset 1). CD47-SIRP α complex (*i.e.*, “Don’t eat me” signal) enables cancer cells to escape phagocytosis by macrophages. CD55 inhibits formation of C3- and C5-convertases, thus indirectly blocking the formation of membrane attack complexes that may degrade the EVs [51]. CD59 interferes directly on the membrane attack complex through its physical incorporation into the complex [52]. Thus, together these antigens can contribute stability, low immunogenicity, and long circulatory availability of EVs [13,14].

Although molecular cloning allows us to express single-chain

variable fragment (scFv) of mAb targeting either PD-1 or PD-L1 on donor cell membranes [53–56], we determined to construct EVs against PD-L1 rather than PD-1 for two reasons. First, a meta-analysis revealed that PD-1 inhibitors are associated with more side effects than PD-L1 inhibitors [57]. Second, it has been widely reported that tumor cell derived oncogenic EVs can deactivate macrophages, NK cells, and T cells through the transfer of encapsulated oncogenic proteins and RNAs [58–60]. Even EVs derived from endothelial cells also can attenuate T cell responses [61]. Therefore, with or without depletion of cargos, engineered EVs targeting PD-1 on T cells may impair T cell biological functions. Therefore, we selected a havPD-1 that is closely related to human wild-type PD-1 and can competitively bind to PD-L1. Before expression of truncated havPD-1 proteins, we knocked out intrinsic PD-L1 proteins in the MDA-MB-231 cell line in order to prevent the simultaneous expression of PD-L1 and havPD-1, which may induce cell and EV agglomeration. Next, we knocked out B2M in order to evade anti-HLA antibodies which may neutralize the EV therapeutic agents. This design was based on recently reported B2M-deficient stem cells and CAR-T cells designed to be universal donors [22,62]. Similarly, we anticipate that B2M-deficient havPD-1 EVs could be a universal donor for EV-based therapy.

We found havPD-1 EVs can inhibit proliferation, migration, and invasion of wild-type MDA-MB-231 cells. In addition, havPD-1 EVs can significantly induce apoptosis in MDA-MB-231 cells. Given that the donor cells double-KO/havPD-1 overexpressing MDA-MB-231 cells themselves are vulnerable to apoptosis and show reduced proliferation, these ripple effects on recipient cells might be further enhanced by cargos encapsulated in havPD-1 EVs. The phenomena may also be associated with intracellular signaling of PD-L1. Recent studies reported PD-L1 blockade may inhibit PD-L1 tumor cell growth by affecting the intracellular MAPK pathway and AKT/mTOR pathway [42,63]. We hypothesize that the derived havPD-1 EVs may have a similar effect. Moreover, drugs targeted against these pathways in combination with immunotherapy targeting PD-L1 may further enhance this effect. Additionally, the high-affinity interaction between havPD-1 and PD-L1 may promote endocytosis of the havPD-1/PD-L1 and the subsequent degradation of PD-L1 [64]. The degradation of PD-L1 may abrogate PD-L1 mediated anti-apoptotic signals to cancer cells due to the fact that PD-L1 itself can enhance cancer cell survival, regulate stress responses, and confer resistance toward pro-apoptotic stimuli without relying on the PD-1 dependent inhibition of T cells [65]. The specific mechanisms of apoptosis and reduced proliferation will be explored in future studies.

Our *in vitro* studies demonstrated havPD-1 EVs lack ADCC and CDC effector functions. They do not trigger T-cell receptor-independent T cell activation but can efficiently block PD-L1 mediated T cell suppression of T cells in an NFAT reporter assay and recall antigen testing assay. In both preventative co-implantation and therapeutic xenograft tumor models reconstituted with human T cells, havPD-1 EVs treatment resulted in robust anti-tumor activity, and the treatment efficacy is comparable to the FDA-approved PD-L1 inhibitor, Atezolizumab. In combination therapy, PD-L1 expressing MDA-MB-436 cells harboring a BRCA1 5396 + 1G > A mutation were treated with Senaparib-loaded havPD-1 EVs. Senaparib is a PARP1/2 inhibitor which significantly inhibits DNA repair and induces synthetic lethality in mutated BRCA1/2 cancers [66]. Of note, a recent study demonstrated that the sno-RNA-PARP-1-DDX21-ribosome biogenesis axis provides an alternative cellular pathway that can be targeted by PARP inhibitors for therapeutic benefits, irrespective of BRCA1/2 status [67]. In our previous study, we investigated the dose-response and treatment efficacy of Senaparib in MDA-MB-436 *in vitro* and *in vivo*. Using this MDA-MB-436 model, we were able to objectively evaluate the effect of low-dose Senaparib-loaded havPD-1 EVs. The senaparib-loaded havPD-1 EVs significantly reduced tumor volume as compared to monotherapy using LD free Senaparib, havPD-1 EVs, or the simple mixture of senaparib and havPD-1 EVs, thus demonstrating that the treatment effect is synergistic when combined into a single agent. Based on this data, we believe that

the enhanced on-tumor delivery of Senaparib using havPD-1 molecules can maximize its treatment efficacy while minimizing its systemic toxicity. The blockade of PD-L1 using havPD-1 can trigger T cell response while simultaneously inducing apoptosis in tumor cells. Moreover, cellular debris, apoptotic bodies, and immunogenic neoantigens derived from apoptotic MDA-MB-436 cells may further activate neoantigen-specific T cells, resulting in a sustained anti-tumor response. It is noteworthy that adverse events of immune checkpoint inhibitors, such as gastrointestinal and hepatic toxicities, kidney infections, pneumonitis, type 1 diabetes, and myocarditis, have been reported. It is unclear whether our engineered havPD-1 EVs derived from tumor cells can induce these above-mentioned side effects and other long-term adverse events. The concerns will be further investigated in our future work. Nevertheless, this proof of principle study demonstrates that havPD-1 EVs could be used for immune checkpoint therapy and show certain superiorities in comparison with FDA approved anti-PD-L1 mAb, Atezolizumab.

Finally, the constructed havPD-1 EVs may inspire new techniques and strategies in cancer immunotherapy. Co-expression of engineered Fc gamma receptors and scFv of mAb targeting tumor-associated antigens, such as HER2, PSMA, GPC3, and GD2 on EV membranes may enhance the antigen blocking effect and antitumor ADCC. Moreover, this work represents a shift from existing EV translational research that primarily focuses on drug delivery and cancer vaccines. It is noteworthy that most current EV-based cancer therapies do not take advantage of many key features of EVs such as their inherent targeting abilities and their ability to deliver membrane-bound proteins. In this study, EVs harboring havPD-1 are used as ICIs and Senaparib nanocarriers. This work opens the door for a variety of therapeutic scenarios, including the ability to overexpress signal-null PD-L1 proteins on donor cells, educate recipient cells with the derived EVs, confer the antigens to recipient cell membranes – each of which may turn immunologically “cold” tumors into “hot” ones. Consequently, the altered cellular phenotype can trigger the infiltrating T cells to recognize and kill tumor cells. Meanwhile, the conferred antigens also allow targeted drug delivery [12]. In addition to the aforementioned potential applications, it is conceivable that engineered EVs harboring biofunctional membrane proteins may serve as therapeutic agents, drug delivery nanocarriers, and/or phenotypic switchers that may have a significant impact on cancer therapeutics.

5. Conclusion

We have engineered havPD-1 overexpressing EVs with potent anti-tumor activity, drug delivery capability, and reduced potential for alloreactivity. These engineered EVs show significant potential as cancer monotherapy and combination therapy to TNBC and related cancers. EVs can be continuously harvested from stable engineered donor cells, thus facilitating the rapid manufacture of clinical-grade EVs and encouraging clinical translation of these off-the-self universal EVs for concurrent immunotherapy and chemotherapy. These therapeutic EVs expand the portfolio of immunotherapeutic agents and deserve further investigation and development.

CRediT authorship contribution statement

Yundi Chen: designed the research, conducted experiments and analyzed data, Writing – original draftwrote the manuscript. **Lixue Wang:** designed the research, conducted experiments and analyzed data. **Mingfeng Zheng:** conducted experiments and analyzed data. **Chuangdong Zhu:** conducted experiments and analyzed data. **Guosheng Wang:** conducted experiments and analyzed data. **Yiqiu Xia:** conducted experiments and analyzed data. **Ethan J. Blumenthal:** conducted experiments and analyzed data. **Wenjun Mao:** designed the research, supervised experiments, Writing – original draftwrote the manuscript. **Yuan Wan:** designed the research, supervised experiments, Writing – original draftwrote the manuscript, All authors reviewed the

manuscript.

Declaration of competing interest

All authors declare that they have no conflicts of interest and no competing interest.

Acknowledgements

Thanks to Dr. L. Nathan Tumey for proofreading the article and suggestions. The work was partially supported by National Cancer Institute (1R01CA230339 subaward and 1R01CA255948), Jiangsu Provincial Medical Youth Talent Award (QNRC2016054), Nanjing Medical Science and Technology Development Foundation Major Program (ZDX16008), Precision Medicine Project of Wuxi Municipal Commission of Health and Family Planning (J201805), the Youth scientific research project of Wuxi municipal health commission (Q201951), and Top Talent Support Program for young and middle-aged people of Wuxi Health Committee (HB2020003).

Appendix A. Supplementary data

Supplementary data to this article can be found online at <https://doi.org/10.1016/j.bioactmat.2021.07.012>.

References

- [1] J. Gong, A. Chehrizi-Raffle, S. Reddi, R. Salgia, Development of PD-1 and PD-L1 inhibitors as a form of cancer immunotherapy: a comprehensive review of registration trials and future considerations, *J. Immunother. Oncol.* 6 (2018).
- [2] J. Sunshine, J.M. Taube, PD-1/PD-L1 inhibitors, *Curr. Opin. Pharmacol.* 23 (2015) 32–38.
- [3] M. Mkrtchyan, Y.G. Najjar, E.C. Raulfs, M.Y. Abdalla, R. Samara, R. Rotem-Yehudar, L. Cook, S.N. Khleif, Anti-PD-1 synergizes with cyclophosphamide to induce potent anti-tumor vaccine effects through novel mechanisms, *Eur. J. Immunol.* 41 (2011) 2977–2986.
- [4] P. Sharma, M. Retz, A. Siefker-Radtke, A. Baron, A. Necchi, J. Bedke, E.R. Plimack, D. Vaena, M.O. Grimm, S. Bracarda, J.A. Arranz, S. Pal, C. Ohya, A. Sazi, X. T. Qu, A. Lambert, S. Krishnan, A. Azrilevich, M.D. Galsky, Nivolumab in metastatic urothelial carcinoma after platinum therapy (CheckMate 275): a multicentre, single-arm, phase 2 trial, *Lancet Oncol.* 18 (2017) 312–322.
- [5] S. Shanda, A.M. Noonan, T.S. Bekaii-Saab, B.H. O’Neil, A. Sehdev, W.L. Shaib, P. R. Helft, P.J. Loehrer, Y. Tong, Z.Y. Liu, B.F. El-Rayes, A phase II study of pembrolizumab in combination with mFOLFOX6 for patients with advanced colorectal cancer, *J. Clin. Oncol.* 35 (2017).
- [6] J. Davda, P. Declerck, S. Hu-Lieskovan, T.P. Hickling, I.A. Jacobs, J. Chou, S. Salek-Ardakani, E. Kraynov, Immunogenicity of immunomodulatory, antibody-based, oncology therapeutics, *J. Immunother. Oncol.* 7 (2019) 105.
- [7] Q. Deveuve, L. Lajoie, B. Barrault, G. Thibault, The proteolytic cleavage of therapeutic monoclonal antibody hinge region: more than a matter of subclass, *Front. Immunol.* 11 (2020).
- [8] L.K. Collins, M.S. Chapman, J.B. Carter, F.H. Samie, Cutaneous adverse effects of the immune checkpoint inhibitors, *Curr. Probl. Canc.* 41 (2017) 125–128.
- [9] C. Thery, L. Zitvogel, S. Amigorena, Exosomes: composition, biogenesis and function, *Nat. Rev. Immunol.* 2 (2002) 569–579.
- [10] Y. Wan, L. Wang, C. Zhu, Q. Zheng, G. Wang, J. Tong, Y. Fang, Y. Xia, G. Cheng, X. He, S.Y. Zheng, Aptamer-conjugated extracellular nanovesicles for targeted drug delivery, *Canc. Res.* 78 (2018) 798–808.
- [11] A. Tan, H. De La Pena, A.M. Seifalian, The application of exosomes as a nanoscale cancer vaccine, *Int. J. Nanomed.* 5 (2010).
- [12] Z. Quinn, W. Mao, Y. Xia, R. John, Y. Wan, Conferring receptors on recipient cells with extracellular vesicles for targeted drug delivery, *Bioact. Mater.* 6 (2021) 749–756.
- [13] S. Kamerkar, V.S. LeBleu, H. Sugimoto, S. Yang, C.F. Ruvio, S.A. Melo, J.J. Lee, R. Kalluri, Exosomes facilitate therapeutic targeting of oncogenic KRAS in pancreatic cancer, *Nature* 546 (2017) 498–503.
- [14] E. Karasu, S.U. Eisenhardt, J. Harant, M. Huber-Lang, Extracellular vesicles: packages sent with complement, *Front. Immunol.* 9 (2018) 721.
- [15] X. Li, A.L. Corbett, E. Taatizadeh, N. Tasnim, J.P. Little, C. Garnis, M. Daugaard, E. Guns, M. Hoorfar, I.T.S. Li, Challenges and opportunities in exosome research—Perspectives from biology, engineering, and cancer therapy, *Appl. Bioeng.* 3 (2019).
- [16] L. Qiao, S.Q. Hu, K. Huang, T. Su, Z.H. Li, A. Vandergriff, J. Cores, P.U. Dinh, T. Allen, D.L. Shen, H.X. Liang, Y.J. Li, K. Cheng, Tumor cell-derived exosomes home to their cells of origin and can be used as Trojan horses to deliver cancer drugs, *Theranostics* 10 (2020) 3474–3487.
- [17] S.G. Antimisiaris, S. Mourtas, A. Marazioti, Exosomes and exosome-inspired vesicles for targeted drug delivery, *Pharmaceutics* 10 (2018).

- [18] D. Ha, N. Yang, V. Nadithe, Exosomes as therapeutic drug carriers and delivery vehicles across biological membranes: current perspectives and future challenges, *Acta Pharm. Sin. B* 6 (2016) 287–296.
- [19] M. Mendt, S. Kamekar, H. Sugimoto, K.M. McAndrews, C.C. Wu, M. Gagea, S. Yang, E.V.R. Blanco, Q. Peng, X. Ma, J.R. Marszalek, A. Maitra, C. Yee, K. Rezvani, E. Shpall, V.S. LeBleu, R. Kalluri, Generation and testing of clinical-grade exosomes for pancreatic cancer, *JCI Insight* 3 (2018).
- [20] H.G. Lamparski, A. Metha-Damani, J.Y. Yao, S. Patel, D.H. Hsu, C. Ruegg, J.B. Le Pecq, Production and characterization of clinical grade exosomes derived from dendritic cells, *J. Immunol. Methods* 270 (2002) 211–226.
- [21] X. Wu, Y. Li, X. Liu, C. Chen, S.M. Harrington, S. Cao, T. Xie, T. Pham, A. S. Mansfield, Y. Yan, E.D. Kwon, L. Wang, K. Ling, H. Dong, Targeting B7-H1 (PD-L1) sensitizes cancer cells to chemotherapy, *Heliyon* 4 (2018), e01039.
- [22] X. Liu, Y. Zhang, C. Cheng, A.W. Cheng, X. Zhang, N. Li, C. Xia, X. Wei, X. Liu, H. Wang, CRISPR-Cas9-mediated multiplex gene editing in CAR-T cells, *Cell Res.* 27 (2017) 154–157.
- [23] S. Jiao, W. Xia, H. Yamaguchi, Y. Wei, M.-K. Chen, J.-M. Hsu, J.L. Hsu, W.-H. Yu, Y. Du, H.-H. Lee, C.-W. Li, C.-K. Chou, S.-O. Lim, S.-S. Chang, J. Litton, B. Arun, G. N. Hortobagyi, M.-C. Hung, PARP inhibitor upregulates PD-L1 expression and enhances cancer-associated immunosuppression, *Clin. Canc. Res.* 23 (2017) 3711–3720.
- [24] R.L. Maute, S.R. Gordon, A.T. Mayer, M.N. McCracken, A. Natarajan, N.G. Ring, R. Kimura, J.M. Tsai, A. Manglik, A.C. Kruse, S.S. Gambhir, I.L. Weissman, A. M. Ring, Engineering high-affinity PD-1 variants for optimized immunotherapy and immuno-PET imaging, *Proc. Natl. Acad. Sci. U. S. A.* 112 (2015) E6506–E6514.
- [25] C.P. Lai, E.Y. Kim, C.E. Badr, R. Weissleder, T.R. Mempel, B.A. Tannous, X. O. Breakefield, Visualization and tracking of tumour extracellular vesicle delivery and RNA translation using multiplexed reporters, *Nat. Commun.* 6 (2015) 7029.
- [26] Y. Wen, Y. Chen, G. Wang, K. Abhange, F. Xue, Z. Quinn, W. Mao, Y. Wan, Factors influencing the measurement of the secretion rate of extracellular vesicles, *Analyst* 145 (2020) 5870–5877.
- [27] Y. Wan, G. Cheng, X. Liu, S.J. Hao, M. Nisic, C.D. Zhu, Y.Q. Xia, W.Q. Li, Z. G. Wang, W.L. Zhang, S.J. Rice, A. Sebastian, I. Albert, C.P. Belani, S.Y. Zheng, Rapid magnetic isolation of extracellular vesicles via lipid-based nanoparticles, *Nat. Biomed. Eng.* 1 (2017).
- [28] C.-d. Zhu, Q. Zheng, L.-x. Wang, H.-f. Xu, J.-l. Tong, Q.-a. Zhang, Y. Wan, J.-q. Wu, Synthesis of novel galactose functionalized gold nanoparticles and its radiosensitizing mechanism, *J. Nanobiotechnol.* 13 (2015) 67.
- [29] J. Bu, A. Nair, M. Iida, W.-j. Jeong, M.J.J. Poellmann, K. Mudd, L.J. Kubiawicz, E. W. Liu, D.L. Wheeler, S. Hong, An avidity-based PD-L1 antagonist using nanoparticle-antibody conjugates for enhanced immunotherapy, *Nano Lett.* 20 (2020) 4901–4909.
- [30] O.P.B. Wiklander, J.Z. Nordin, A. O’Loughlin, Y. Gustafsson, G. Corso, I. Mager, P. Vader, Y. Lee, H. Sork, Y. Seow, N. Heldring, L. Alvarez-Erviti, C.I.E. Smith, K. Le Blanc, P. Macchiarini, P. Jungbluth, M.J.A. Wood, S. EL Andaloussi, Extracellular vesicle in vivo biodistribution is determined by cell source, route of administration and targeting, *J. Extracell. Vesicles* 4 (2015).
- [31] B.K. Matuszewski, M.L. Constanzer, C.M. Chavez-Eng, Strategies for the assessment of matrix effect in quantitative bioanalytical methods based on HPLC-MS/MS, *Anal. Chem.* 75 (2003) 3019–3030.
- [32] X.D. Wang, X.H. Yang, C. Zhang, Y. Wang, T.Y. Cheng, L.Q. Duan, Z. Tong, S. G. Tan, H.J. Zhang, P.E. Saw, Y.M. Gu, J.H. Wang, Y.B. Zhang, L.N. Shang, Y.J. Liu, S.Y. Jiang, B.X. Yan, R. Li, Y. Yang, J. Yu, Y.Z. Chen, G.F. Gao, Q.N. Ye, S. Gao, Tumor cell-intrinsic PD-1 receptor is a tumor suppressor and mediates resistance to PD-1 blockade therapy, *Proc. Natl. Acad. Sci. USA* 117 (2020) 6640–6650.
- [33] R.S. Herbst, J.C. Soria, M. Kowanetz, G.D. Fine, O. Hamid, M.S. Gordon, J. A. Sosman, D.F. McDermott, J.D. Powderly, S.N. Gettinger, H.E.K. Kohrt, L. Horn, D.P. Lawrence, S. Rost, M. Leabman, Y.Y. Xiao, A. Moktrin, H. Koeppen, P. S. Hegde, I. Mellman, D.S. Chen, F.S. Hodi, Predictive correlates of response to the anti-PD-L1 antibody MPDL3280A in cancer patients, *Nature* 515 (2014) 563–+.
- [34] G. Chen, A.C. Huang, W. Zhang, G. Zhang, M. Wu, W. Xu, Z.L. Yu, J.G. Yang, B. K. Wang, H.H. Sun, H.F. Xia, Q.W. Man, W.Q. Zhong, L.F. Antelo, B. Wu, X. P. Xiong, X.M. Liu, L. Guan, T. Li, S.J. Liu, R.F. Yang, Y.T. Lu, L.Y. Dong, S. McGettigan, R. Somasundaram, R. Radhakrishnan, G. Mills, Y.L. Lu, J. Kim, Y.H. H. Chen, H.D. Dong, Y.F. Zhao, G. K. Karakousis, T.C. Mitchell, L.M. Schuchter, M. Herlyn, E.J. Wherry, X.W. Xu, W. Guo, Exosomal PD-L1 contributes to immunosuppression and is associated with anti-PD-1 response, *Nature* 560 (2018) 382–+.
- [35] Y. Yang, C.W. Li, L.C. Chan, Y.K. Wei, J.M. Hsu, W.Y. Xia, J.H. Cha, J.W. Hou, J. L. Hsu, L.L. Sun, M.C. Hung, Exosomal PD-L1 harbors active defense function to suppress T cell killing of breast cancer cells and promote tumor growth, *Cell Res.* 28 (2018) 862–864.
- [36] X.D. Xie, H.F. Nie, Y. Zhou, S. Lian, H. Mei, Y.S. Lu, H.Y. Dong, F.Q. Li, T. Li, B. F. Li, J. Wang, M. Lin, C.H. Wang, J.W. Shao, Y. Gao, J.M. Chen, F.W. Xie, L. Jia, Eliminating blood oncogenic exosomes into the small intestine with aptamer-functionalized nanoparticles (vol 10, 5476, 2019), *Nat. Commun.* 11 (2020).
- [37] J.J. Orme, E.A.L. Enninga, F. Lucien-Matteoni, H. Dale, E. Burgstaler, S. M. Harrington, M.K. Ball, A.S. Mansfield, S.S. Park, M.S. Block, S.N. Markovic, Y. Y. Yan, H.D. Dong, R.S. Dronca, J.L. Winters, Therapeutic plasma exchange clears circulating soluble PD-L1 and PD-L1-positive extracellular vesicles, *J. Immunother. Canc.* 8 (2020).
- [38] M. Poggio, T.Y. Hu, C.C. Pai, B. Chu, C.D. Belair, A. Chang, E. Montabana, U. E. Lang, Q. Fu, L. Fong, R. Blueloch, Suppression of exosomal PD-L1 induces systemic anti-tumor immunity and memory, *Cell* 177 (2019) 414–+.
- [39] H. Ghebeh, C. Lehe, E. Barhoush, K. Al-Romaih, A. Tulbah, M. Al-Alwan, S. F. Hendrayani, P. Manogaran, A. Alaiya, T. Al-Tweigeri, A. Abousekhra, S. Dermime, Doxorubicin downregulates cell surface B7-H1 expression and upregulates its nuclear expression in breast cancer cells: role of B7-H1 as an anti-apoptotic molecule, *Breast Cancer Res.* 12 (2010).
- [40] S. Jiao, W. Xia, H. Yamaguchi, Y. Wei, M.K. Chen, J.M. Hsu, J.L. Hsu, W.H. Yu, Y. Du, H.H. Lee, C.W. Li, C.K. Chou, S.O. Lim, S.S. Chang, J. Litton, B. Arun, G. N. Hortobagyi, M.C. Hung, PARP inhibitor upregulates PD-L1 expression and enhances cancer-associated immunosuppression, *Clin. Canc. Res.* 23 (2017) 3711–3720.
- [41] R. Saleh, R.Z. Taha, V. Sasidharan Nair, N.M. Alajez, E. Elkord, PD-L1 blockade by Atezolizumab downregulates signaling pathways associated with tumor growth, metastasis, and hypoxia in human triple negative breast cancer, *Cancers* (2019) 11.
- [42] M. Passariello, A.M. D’Alise, A. Esposito, C. Vetrei, G. Froechlich, E. Scarselli, A. Nicosia, C. De Lorenzo, Novel human anti-PD-L1 mAbs inhibit immune-independent tumor cell growth and PD-L1 associated intracellular signalling, *Sci. Rep. UK* 9 (2019).
- [43] J. Cao, P. Zhang, P.L.d. Souza, B. Gao, M. Voskoboinik, D. Ji, W. Shen, S. Yang, Y. Zhou, R. Zhang, J.D. Lickliter, S.-N. Hoon, D. Palmieri, S. Cai, Y.E. Tian, N. Ma, C. Xu, S. Yang, S. Zhang, B. Xu, Pooled analysis of phase I dose-escalation and dose cohort expansion studies of IMP4297, a novel PARP inhibitor, in Chinese and Australian patients with advanced solid tumors, *J. Clin. Oncol.* 37 (2019), 3059–3059.
- [44] J.P.W. Carey, C. Karakas, T.Y. Bui, X. Chen, S. Vijayaraghavan, Y. Zhao, J. Wang, K. Mikule, J.K. Litton, K.K. Hunt, K. Keyomarsi, Synthetic lethality of PARP inhibitors in combination with MYC blockade is independent of BRCA status in triple-negative breast cancer, *Canc. Res.* 78 (2018) 742–757.
- [45] J.D.C. Hon, B. Singh, A. Sahin, G. Du, J.H. Wang, V.Y. Wang, F.M. Deng, D. Y. Zhang, M.E. Monaco, P. Lee, Breast cancer molecular subtypes: from TNBC to QNBC, *Am. J. Canc. Res.* 6 (2016) 1864–1872.
- [46] P. Vikas, N. Borcherding, W. Zhang, The clinical promise of immunotherapy in triple-negative breast cancer, *Canc. Manag. Res.* 10 (2018) 6823–6833.
- [47] E.A. Mittendorf, A.V. Phillips, F. Meric-Bernstam, N. Qiao, Y. Wu, S. Harrington, X. P. Su, Y. Wang, A.M. Gonzalez-Angulo, A. Akcakanat, A. Chawla, M. Curran, P. Hwu, P. Sharma, J.K. Litton, J.J. Mouldrem, G. Alatrash, PD-L1 expression in triple-negative breast cancer, *Canc. Immunol. Res.* 2 (2014) 361–370.
- [48] P. Garcia-Tejido, M.L. Cabal, I.P. Fernandez, Y.F. Perez, Tumor-infiltrating lymphocytes in triple negative breast cancer: the future of immune targeting, *Clin. Med. Insights Oncol.* 10 (2016) 31–39.
- [49] M.N. Wang, Y. Liu, Y. Cheng, Y.Q. Wei, X.W. Wei, Immune checkpoint blockade and its combination therapy with small-molecule inhibitors for cancer treatment, *Bba-Rev. Canc.* 1871 (2019) 199–224.
- [50] J.B.A.G. Haanen, Converting cold into hot tumors by combining immunotherapies, *Cell* 170 (2017) 1055–1056.
- [51] D.M. Lublin, J.P. Atkinson, Decay-accelerating factor: biochemistry, molecular biology, and function, *Annu. Rev. Immunol.* 7 (1989) 35–58.
- [52] I. Farkas, L. Baranyi, Y. Ishikawa, N. Okada, C. Bohata, D. Budai, A. Fukuda, M. Imai, H. Okada, CD59 blocks not only the insertion of C9 into MAC but inhibits ion channel formation by homologous C5b-8 as well as C5b-9, *J. Physiol.* 539 (2002) 537–545.
- [53] A. Longatti, C. Schindler, A. Collinson, L. Jenkinson, C. Matthews, L. Fitzpatrick, M. Blundy, R. Minter, T. Vaughan, M. Shaw, N. Tighe, High affinity single-chain variable fragments are specific and versatile targeting motifs for extracellular vesicles, *Nanoscale* 10 (2018) 14230–14244.
- [54] X. Zou, M. Yuan, T. Zhang, H. Wei, S. Xu, N. Jiang, N. Zheng, Z. Wu, Extracellular vesicles expressing a single-chain variable fragment of an HIV-1 specific antibody selectively target Env(+) tissues, *Theranostics* 9 (2019) 5657–5671.
- [55] F. Ferrantelli, C. Arenaccio, F. Manfredi, E. Olivetta, C. Chiozzini, P. Leone, Z. Percario, A. Ascione, M. Flego, P. Di Bonito, L. Accardi, M. Federico, The intracellular delivery of anti-HPV16 E7 scFvs through engineered extracellular vesicles inhibits the proliferation of HPV-infected cells, *Int. J. Nanomed.* 14 (2019) 8755–8768.
- [56] I.V. Balyasnikova, R. Franco-Gou, J.M. Mathis, M.S. Lesniak, Genetic modification of mesenchymal stem cells to express a single-chain antibody against EGFRvIII on the cell surface, *J. Tissue Eng. Regen. M* 4 (2010) 247–258.
- [57] T.F. Nishijima, S.S. Shachar, K.A. Nyrop, H.B. Muss, Safety and tolerability of PD-1/PD-L1 inhibitors compared with chemotherapy in patients with advanced cancer: a meta-analysis, *Oncol.* 22 (2017) 470–479.
- [58] L. Mincheva-Nilsson, V. Baranov, Cancer exosomes and NKG2D receptor–ligand interactions: impairing NKG2D-mediated cytotoxicity and anti-tumour immune surveillance, *Semin. Canc. Biol.* 28 (2014) 24–30.
- [59] M.S. Baig, A. Roy, S. Rajpoot, D. Liu, R. Savai, S. Banerjee, M. Kawada, S.M. Faisal, R. Saluja, U. Saqib, T. Ohishi, K.K. Wary, Tumor-derived exosomes in the regulation of macrophage polarization, *Inflamm. Res.* 69 (2020) 435–451.
- [60] J. Wolfers, A. Lozier, G. Raposo, A. Regnault, C. Thery, C. Masurier, C. Flament, S. Pouzieux, F. Faure, T. Tursz, E. Angevin, S. Amigorena, L. Zitvogel, Tumor-derived exosomes are a source of shared tumor rejection antigens for CTL cross-priming, *Nat. Med.* 7 (2001) 297–303.
- [61] M.S. Njock, H.S. Cheng, L.T. Dang, M. Nazari-Jahantigh, A.C. Lau, E. Boudreau, M. Roufaiel, M.I. Cybulsky, A. Schober, J.E. Fish, Endothelial cells suppress monocyte activation through secretion of extracellular vesicles containing antiinflammatory microRNAs, *Blood* 125 (2015) 3202–3212.
- [62] S. Mattapally, K.M. Pawlik, V.G. Fast, E. Zumaquero, F.E. Lund, T.D. Randall, T. M. Townes, J. Zhang, Human leukocyte antigen class I and II knockout human induced pluripotent stem cell-derived cells: universal donor for cell therapy, *J. Am. Heart Assoc.* 7 (2018), e010239.

- [63] C.S. Palmer, M. Ostrowski, B. Balderson, N. Christian, S.M. Crowe, Glucose metabolism regulates T cell activation, differentiation, and functions, *Front. Immunol.* 6 (2015) 1.
- [64] Q. Gou, C. Dong, H.H. Xu, B. Khan, J.H. Jin, Q. Liu, J.J. Shi, Y.Z. Hou, PD-L1 degradation pathway and immunotherapy for cancer, *Cell Death Dis.* 11 (2020).
- [65] T. Azuma, S. Yao, G. Zhu, A.S. Flies, S.J. Flies, L. Chen, B7-H1 is a ubiquitous antiapoptotic receptor on cancer cells, *Blood* 111 (2008) 3635–3643.
- [66] K.N. Dziadkowiec, E. Gasiorowska, E. Nowak-Markwitz, A. Jankowska, PARP inhibitors: review of mechanisms of action and BRCA1/2 mutation targeting, *Menopausal Rev.* 15 (2016) 215–219.
- [67] D.S. Kim, C.V. Camacho, A. Nagari, V.S. Malladi, S. Challa, W.L. Kraus, Activation of PARP-1 by snoRNAs controls ribosome biogenesis and cell growth via the RNA helicase DDX21, *Mol. Cell.* 75 (2019) 1270–1285, e1214.